Chapter 6

Inclusive experimental results

This chapter covers the presentation of the results of the inclusive measurements for hard photons and charged particles. In the first two sections I will focus on the analysis of the measured hard photon energy spectrum and the angular emission distribution. Next, the features of the charged particle distributions measured in the Dwarf Ball and in the Forward Wall are discussed. In Section 6.4 the results concerning reaction and hard photon cross-sections and related hard photon measurements are presented. In the last section, I will discuss the new systematics built with the experimental data collected from the different experiments where a thermal hard photon component has been clearly identified and measured.

6.1 Photon energy measurements

Inclusive photon spectra result from the sum of contributions from all the photon production processes, without requiring any particular final state of the nuclear reaction. The corresponding events have been selected by requiring that they have fired the photon minimum bias trigger. In our set-up this is the "Neutral*DB1" trigger, which signals events where a photon of energy $E_\gamma > 10$ MeV in TAPS is in coincidence with a charged particle detected in the Dwarf Ball. The selection of such a "photon-particle" coincidence to analyze photon inclusive measurements guarantees the occurrence of a photon emission during a real nuclear reaction. Thus, "photon" contributions coming from false events, mainly cosmic rays firing any or several TAPS modules, are minimized.

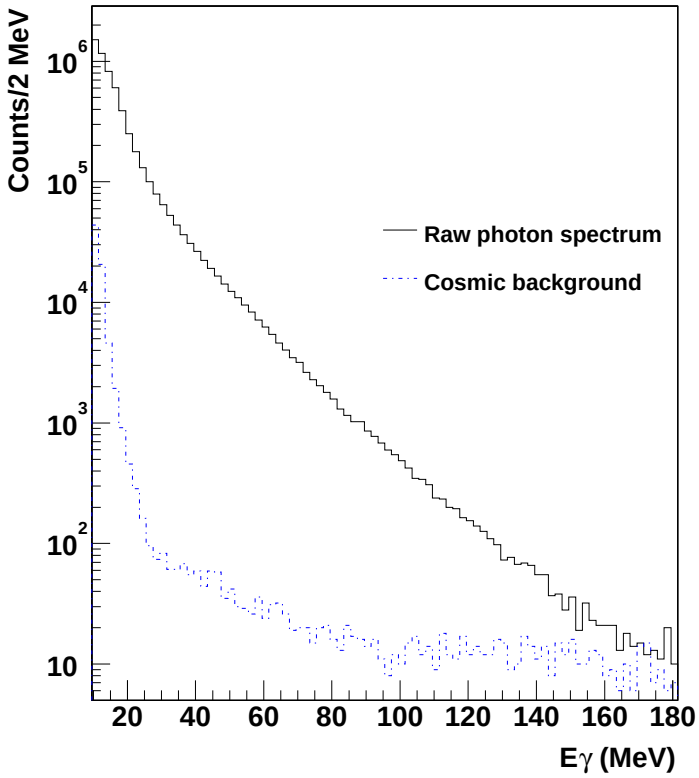

Figure 6.1: *Experimental inclusive raw photon spectrum measured in the NN center-of-mass frame for the reaction ^{129}Xe + ^{nat}Sn at 50A MeV. The dashed line represents the cosmic ray background contribution.*

6.1.1 Raw photon spectrum

In Fig. 6.1 we present the inclusive raw photon energy spectrum for the ^{129}Xe + ^{nat}Sn reaction at 50A MeV, constructed from the collection of $5.8 \cdot 10^6$ photons of $E_\gamma > 10$ MeV measured in TAPS and transformed into the nucleon-nucleon (NN) center-of-mass frame,

$$E_\gamma^{NN} = \gamma_{NN} E_\gamma^{lab} (1 - \beta_{NN} \cos\theta_\gamma^{lab}) \quad \text{with } \beta_{NN} = 0.16 \quad \text{and } \gamma_{NN} = 1.012 \qquad (6.1)$$

Subtraction of the cosmic ray contribution

The probability to detect a hard-photon is comparable to that of recording a cosmic muon during a nuclear reaction in the high energy region of the spectrum. Although the trigger has been selected to minimize the cosmic ray contamination, we therefore have to reject this contribution in order to completely avoid a photon misidentification. This is why in the particle identification step we have chosen to characterize the cosmic ray

events according to the same time-of-flight and pulse-shape windows used in the photon identification (see Table 4.1). This selection permits to subtract the contribution of cosmic ray events from the raw photon spectrum, in order to construct properly the inclusive spectrum of emitted photons from the nuclear reaction. The background of the 2 photon electromagnetic decay of neutral pions produced in the reaction is at this bombarding energy marginal.

6.1.2 Hard photon energy analysis

In agreement with the former analysis performed by the TAPS collaboration discussed in section 2.3, we have found that the inclusive hard photon energy spectrum of the Xe+Sn reaction at $50A$ MeV cannot be well described by just one exponential distribution, due to an excess of the hard-photon yield in the energy region of 30 - 60 MeV. This excess then calls for the existence of a second hard-photon contribution. The contribution of each source can be extracted after the fit of the data with the following function:

$$\frac{dN}{dE_\gamma} = K_d\, e^{-E_\gamma/E_0^d} + K_t\, e^{-E_\gamma/E_0^t} \tag{6.2}$$

where d and t stand for direct and thermal, respectively, and the factors K are related to the intensity of each source:

$$I_{d(t)} = K_{d(t)} \int_{E_{thr}=30MeV}^{\infty} e^{-E_\gamma/E_0^{d(t)}} dE_\gamma = K_{d(t)}\, E_0^{d(t)}\, e^{-30/E_0^{d(t)}} \tag{6.3}$$

The low energy threshold of the fit, 30 MeV, has been selected in a conservative way, as already advocated in the previous analysis of the KVI experiment [26], in order to minimize any possible photon background from the tail of the GDR photon distribution. The effective upper limit corresponds to the most energetic possible case of pnγ bremsstrahlung, the so-called "kinematic limit" for bremsstrahlung $E_\gamma^{max}(s)$: a photon of energy is created in a head-on collision where both nucleons having the maximum intrinsic Fermi momentum, $p_F = 270$ MeV. In that case, we have:

$$E_\gamma^{max}(s) = \frac{s_{max} - 4m_N^2}{2\sqrt{s_{max}}} = 181 \quad \text{MeV} \tag{6.4}$$

where $s_{max} = 2\frac{[E_F(m_N+E_{lab}) + p_F\, p_{lab}]^2}{m_N\,(m_N+E_{lab})}$ is the maximum energy available in a pn collision, $E_F = \sqrt{p_F^2 + m_N^2}$ and $E_{lab} = K_{lab} + m_N$.

The result of the double source fit of the inclusive energy hard photon spectrum is displayed in Fig. 6.2 and the parameters obtained in the least square fit are reported in

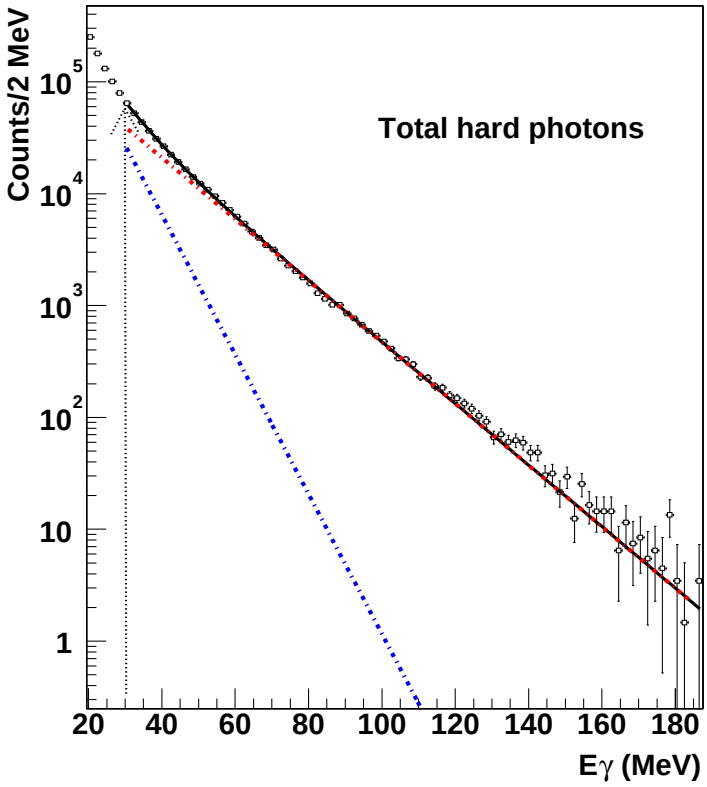

Figure 6.2: *Experimental inclusive hard photon spectrum measured for the reaction* $^{129}Xe + ^{nat}Sn$ *at 50A MeV in the NN center-of-mass frame. The spectrum has been fitted according to the double exponential distribution of Eq. 6.2 in the energy range* E_γ *= 30 - 180 MeV. The thermal (dashed line) and direct (solid line) exponential contributions are shown.*

E_0^d (MeV)	E_0^t (MeV)	I_t/I_{tot}(%)	χ^2/ndf
15.6 ± 1.0	7.0 ± 0.6	22 ± 1	1.9

Table 6.1: *Thermal and direct slopes and ratio of thermal to total intensities deduced from the inclusive spectrum measured for the reaction* $^{129}Xe + ^{nat}Sn$ *at 50A MeV (see Fig. 6.2).*

Table 6.1. The associated errors are obtained by combining in quadrature the statistical and systematical errors.

The softer hard-photon distribution, with inverse slope parameter $E_0^t = (7.0 \pm 0.6)$ MeV, corresponds to the thermal hard component and the harder one, $E_0^d = (15.6 \pm 1.0)$, accounts for the dominant direct hard-photon production. The existence of these two

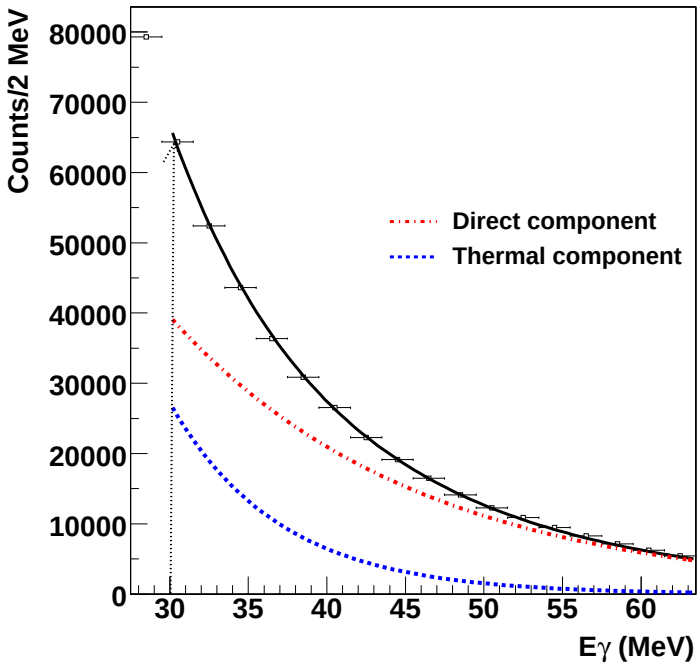

Figure 6.3: *The measured hard-photon energy spectrum in the region $E_\gamma = 30$ - 65 MeV plotted in a linear scale to emphasize the existence of the two different hard-photon contributions.*

different components can be still best appreciated in Figs. 6.3 and 6.4. The systematics of the direct and thermal slopes is discussed in sections 6.5 and 6.6, respectively.

The thermal contribution in the energy range of 30 - 60 MeV amounts to 22% of the total hard-photon intensity [thermal and direct intensities have been calculated according to Eq. (6.3)]. This ratio is compatible with those measured for the heaviest and the most symmetric systems reported in Table 6.8. This result confirms that the largest measured thermal bremsstrahlung yields, $I_t/I_{tot} \sim 20\%$, are obtained in heavy and symmetric reactions, in which the number of participant nucleons and the attained excitation energy are high enough to produce a secondary NN bremsstrahlung. We have also measured the percentage of thermal hard photons with respect to the total yield for different energy subranges within the 30 - 60 MeV region (Table 6.2). The observed I_t/I_{tot} evolution verifies the fact that the thermal photon production becomes less important when the hard photon energy increases. Thus, above $E_\gamma > 60$ MeV only the direct hard-photon emission remains. A typical procedure to check the consistence of the double-source anal-

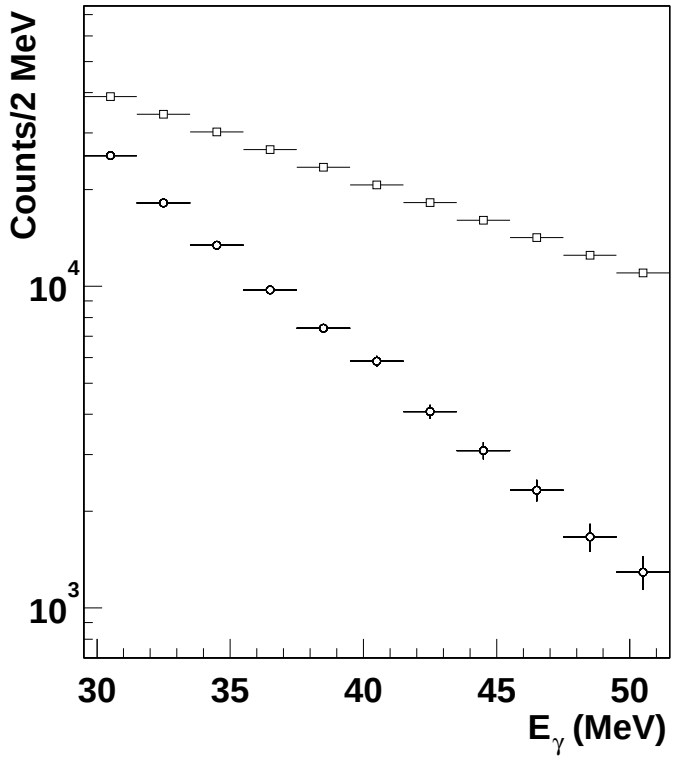

Figure 6.4: *The measured thermal (circles) and direct (squares) exponential hard-photon distributions are explicitly shown. The thermal (direct) component has been obtained after subtracting the direct (thermal) contribution from the total experimental inclusive spectrum.*

Energy range	I_t/I_{tot}
(30 - 35) MeV	38% ± 1%
(35 - 40) MeV	29% ± 1%
(40 - 45) MeV	22% ± 1%
(45 - 50) MeV	14% ± 1%
(50 - 55) MeV	9% ± 2%
(55 - 60) MeV	5% ± 2%

Table 6.2: *Ratios of thermal to total hard-photon intensities measured in different energy ranges.*

ysis consists in analyzing the spectrum measured at $\theta_\gamma^{lab} = 90°$, for which $E_\gamma^{90°} \approx E_\gamma^{lab}$. To minimize any kinematic effect on the hard-photon excess observed in the low energy range of the spectrum, the values of the parameters of the double fit of the spectrum

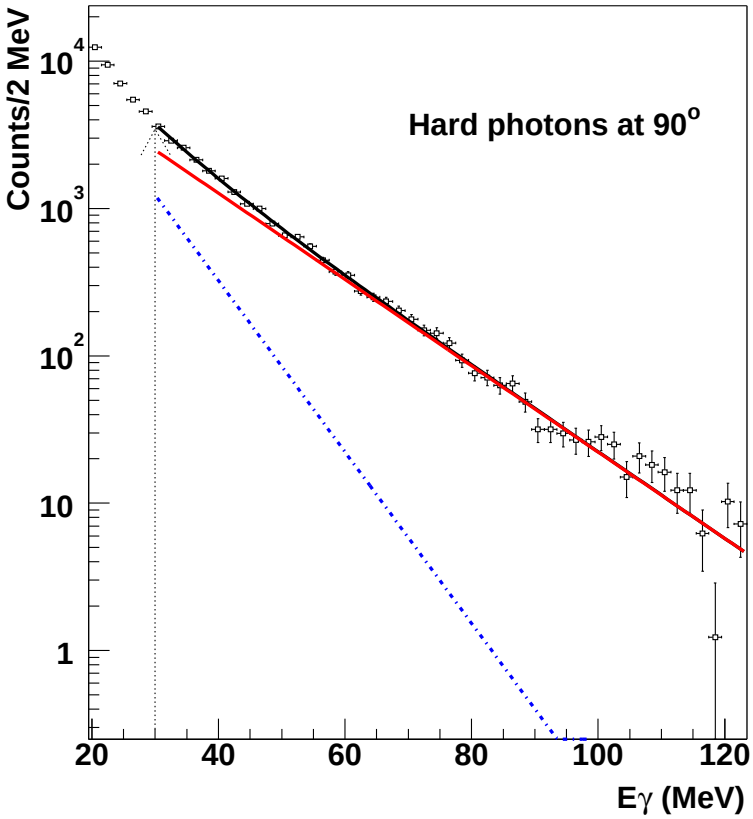

Figure 6.5: *Inclusive hard photon spectrum measured at* $\theta_{lab} = 90° \pm 3°$. *The spectrum has been fitted in the region* E_γ = *30 - 125 MeV according to Eq. (6.2).*

distribution integrated over θ_{lab} and those of the spectrum at 90° shouldn't differ much. The fit of our inclusive spectrum centered at 90° ($87° < \theta_{lab} < 93°$) according to Eq. (6.2) (see Fig. 6.5) has led to the slope and intensity parameters reported in Table 6.3. The compatibility of these values and those found in the total hard photon spectrum of Table 6.1 validates the previous analysis. Moreover, the individual photon energy spectrum

E_0^d (MeV)	E_0^t (MeV)	I_t/I_{tot}(%)	χ^2/ndf
15.1 ± 1.1	7.6 ± 0.9	22 ± 1	1.1

Table 6.3: Direct and thermal slopes and ratio of thermal to total intensities deduced from the hard photon spectrum measured at $\theta_{lab} = 90° \pm 3°$.

measured in each TAPS block has also been analyzed in order to search for any possible

Block	E_0^d (MeV)	E_0^t (MeV)	I_t/I_{tot}(%)	χ^2/ndf
A	15.5 ± 1.2	5.9 ± 0.9	16% ± 3%	2.2
F	16.3 ± 1.0	5.8 ± 0.7	18% ± 1%	1.2
B	15.1 ± 1.0	7.0 ± 0.7	22% ± 1%	1.0
E	15.7 ± 1.2	6.9 ± 0.8	24% ± 2%	1.4
C	15.5 ± 1.1	5.7 ± 0.9	17% ± 2%	1.2
D	15.6 ± 1.0	6.4 ± 0.8	20% ± 1%	1.0

Table 6.4: *Direct and thermal slopes and the ratio of thermal to total hard-photon intensities measured in each TAPS block.*

deviation. Therefore, the six hard-photon distributions have been fitted according to Eq. (6.2) in the energy region 30 - 145/150 MeV, the extracted parameters are listed in Table 6.4. The ratios of thermal to total intensities and direct and thermal slopes agree, within their respective errors, with those of the total hard-photon spectrum, reflecting the good response of all six TAPS blocks. The differences between the values are solely explaneable as due to the angular position of the (pairs of) blocks.

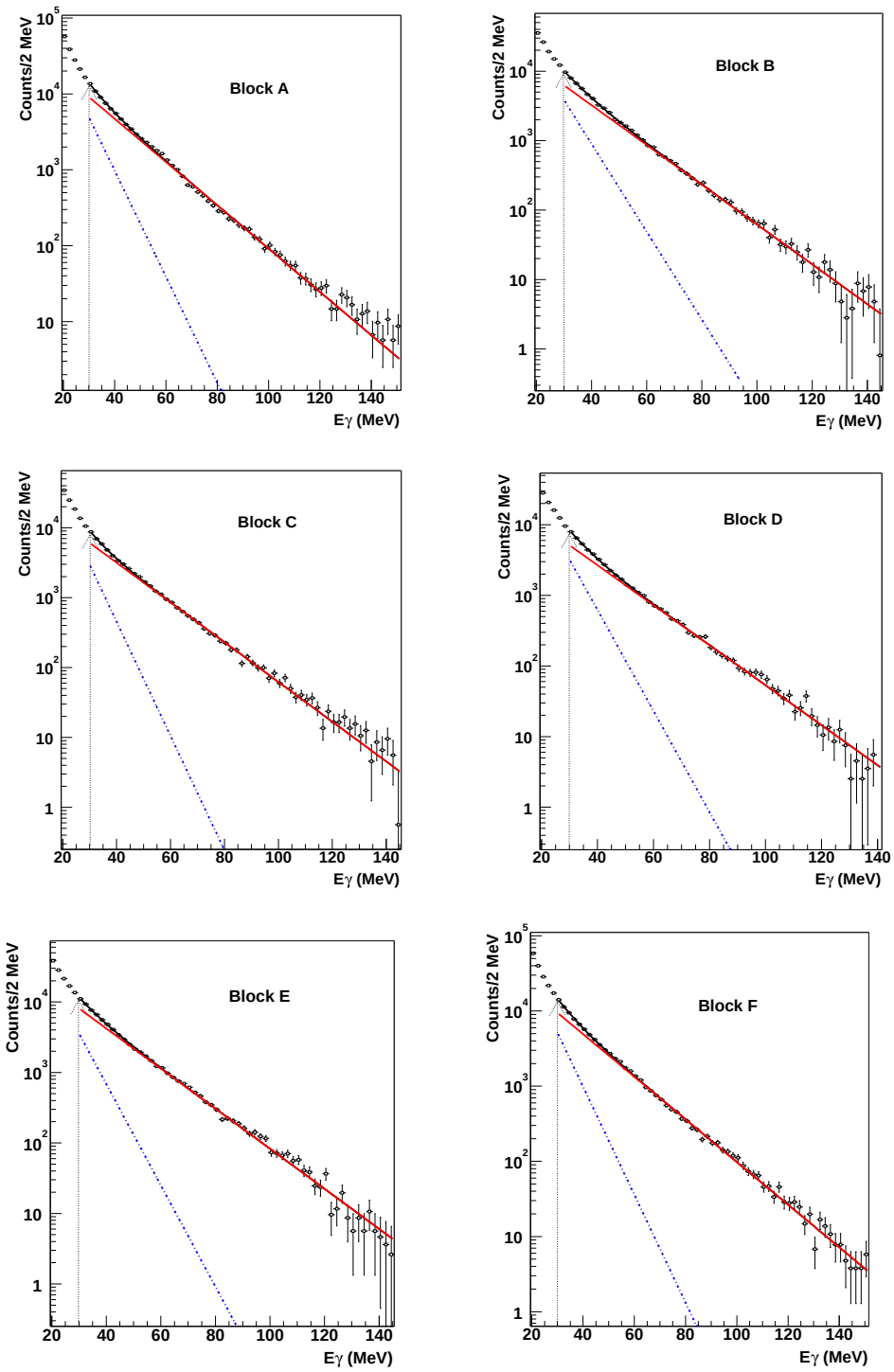

Figure 6.6: *The experimental inclusive hard photon energy spectra measured in each TAPS block. The spectra have been fitted according to Eq. (6.2) in the energy range E_γ = 30 - 145/150 MeV. The thermal (dashed line) and direct (solid line) exponential distributions are also displayed.*

6.2 Analysis of the hard-photon angular distribution

We have seen in Section 2.2 that the velocity of the hard-photon source can be extracted from the angular distribution measured in the laboratory frame by means of the Doppler effect. Thus, the analysis of the hard-photon angular emission investigated in the asymmetric projectile-target systems studied in the KVI experiment (^{36}Ar+^{197}Au, ^{107}Ag, ^{58}Ni and ^{12}C at 60A MeV) has demonstrated that whereas direct photons are emitted from a source moving with a velocity $\beta \approx \beta_{NN}$, the thermal hard photon component is emitted isotropically from a source with a velocity close to that of the AA center-of-mass one [26]. These results confirm that direct and thermal photons originate from individual first chance and from secondary NN collisions, respectively.

In our experiment the existence of the two different hard-photon distributions has been already demonstrated in the previous section by the double source analysis of the hard photon energy spectrum. However, due to the close mass symmetry of the ^{129}Xe+^{nat}Sn system, the nucleon-nucleon and the nucleus-nucleus center-of-mass velocities are practically equal, $\beta_{NN} = 0.157$ and $\beta_{AA} = 0.164$, and the small difference between both velocities cannot be ascertained within the experimental uncertainties. Therefore, unlike in former experiments performed with asymmetric reactions, here the extracted values of the hard-photon source velocities will not allow to prove the different origin of the direct and thermal hard-photon components. Nevertheless, the analysis of the measured laboratory hard photon angular distribution, $\frac{dN_\gamma}{d\Omega}$, is important in order to test the consistency of the previous energy spectrum analysis. Moreover, besides the velocity of the emitting source, there is another observable sensitive to the origin of the hard photon emission which can be extracted from the measured laboratory angular spectra. This is the *anisotropy dipole factor (α)* of Eq. (2.5) whose existence, as it has been discussed in 2.2, can only be related with the photon emission in the first pn collisions. However, as we will see below, the extraction of α from the experimental angular distribution can only be considered, due to the systematic uncertainties, as an estimation.

The relative yield of direct and thermal hard photons depends on the measured energy range (see Table 6.2). In order to investigate this energy dependence we have studied the laboratory angular distribution in 4 different energy domains:

1. 30 MeV $<$ E$_\gamma$ $<$ 40 MeV;

2. 30 MeV $<$ E$_\gamma$ $<$ 60 MeV;

3. $E_\gamma > 60$ MeV;

4. The full hard photon angular distribution, $E_\gamma > 30$ MeV.

6.2.1 Angular distributions for different energy ranges

The hard photon distributions for the 30 MeV$<$ E$_\gamma$ $<$40 MeV and $E_\gamma > 60$ MeV regions exhibit particularly interesting features (see Table 6.2). On the one hand, the first case consists of a mixed distribution of direct and thermal photons and the thermal component exhibits its largest contribution in this energy range. On the other hand, photons of energies above 60 MeV have only a direct origin (see Table 6.2).

The measured laboratory angular distributions integrated over the three energy subranges of 30 MeV$<$ E$_\gamma$ $<$40 MeV, 30 MeV$<$ E$_\gamma$ $<$60 MeV and $E_\gamma > 60$ MeV have been fitted according to the following expression [1]:

$$\left(\frac{dN}{d\Omega}\right)_{lab} = \frac{K}{Z^2}\left[1-\alpha+\alpha\,\frac{\sin^2\theta_\gamma^{lab}}{Z^2}\right] E_0^{local}\left[e^{-E_{min}\cdot Z/E_0} - e^{-E_{max}\cdot Z/E_0}\right] \qquad (6.5)$$

with the Lorentz factor: $Z = \gamma_S\,(1-\beta_S\cos\theta_{lab})$, α is the anisotropy factor, low energy thresholds E_{min} = (30,40 and 60 MeV) and high energy thresholds E_{max} = (40,60 and ∞ MeV). The value of the (local) inverse slope E_0 is extracted from the measured laboratory energy spectrum and K is deduced from the laboratory angular distribution measured at $\theta^{lab} = 90°$. Only the α and β_S parameters are left free. The results for the fits of the angular distributions measured in the three consecutive energy subranges are plotted in Figures 6.7, 6.8 and 6.9. Table 6.5 reports the values of the α and β_S parameters obtained in the least-χ^2 fits.

Source velocity: As expected the values of the velocity of the hard-photon source β_S extracted in all three fits are nearly equal and agree with the value expected from the emission by a source moving with $\beta_S \approx \beta_{NN}$ but also with $\beta_S \approx \beta_{AA}$.

Anisotropy factor: As we have discussed in the second chapter, the measurement of a dipole component (a non-zero anisotropy factor) can only be related with radiation emerging from first-chance NN scattering, in which the momentum of the projectile nucleon still conserves its original direction. In our analysis, we observe a non zero anisotropy factor,

[1] This angular distribution comes directly from the energy integration of Eq.(2.6)

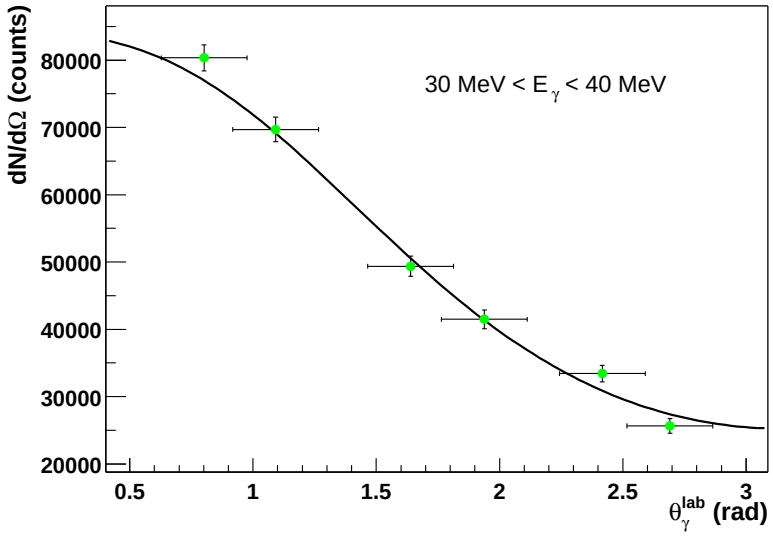

Figure 6.7: *Experimental angular distribution measured in the laboratory frame for photons of energies in the region 30 MeV< E_γ <40 MeV. The solid line represents the result of a fit with Eq. (6.5).*

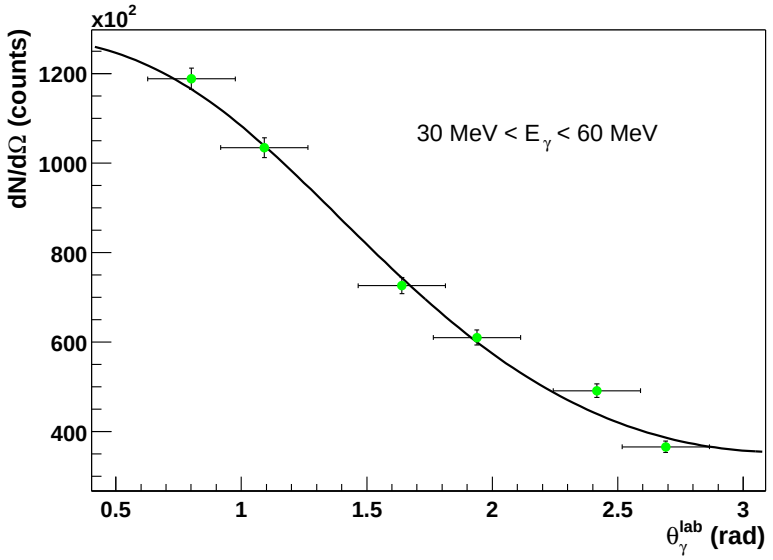

Figure 6.8: *Experimental angular distribution measured in the laboratory frame for photons of energies in the region 30 MeV< E_γ <60 MeV. The solid line represents the result of a fit with Eq. (6.5).*

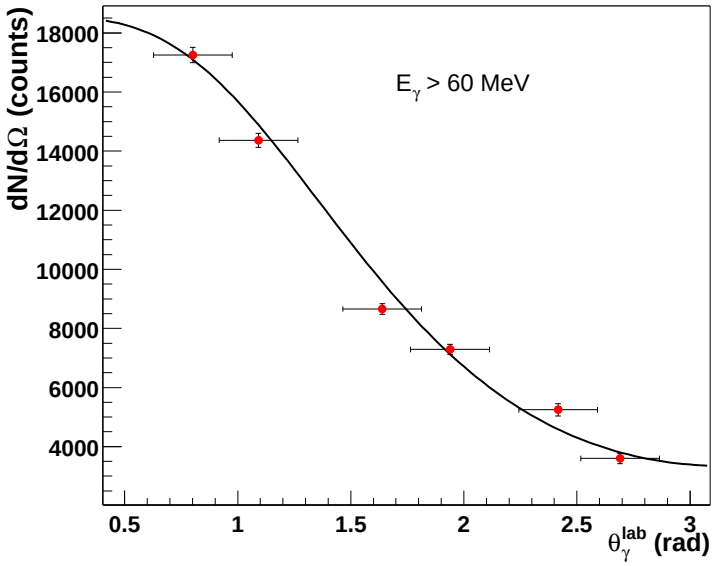

Figure 6.9: *Experimental angular distribution measured in the laboratory frame for photons of energies in the region $E_\gamma > 60$ MeV. The solid line represents the result of a fit with Eq. (6.5).*

Energy range	β_S	α	χ^2/ndf	E^{local} (MeV)
30 MeV < E_γ < 40 MeV	0.15 ± 0.01	0.0 ± 0.1	1.0	12.5 ± 0.7
30 MeV < E_γ < 60 MeV	0.16 ± 0.01	0.1 ± 0.1	0.7	11.1 ± 0.8
E_γ > 60 MeV	0.16 ± 0.01	0.2 ± 0.1	0.5	15.1 ± 1.0

Table 6.5: *Values of source velocities and anisotropy factors obtained from the fits with Eq. 6.5 of the experimental laboratory angular distributions measured in 3 different energy ranges. The local slopes E^{local} extracted from the fits are also reported.*

$\alpha = 0.2 \pm 0.1$, in the energy region of $E_\gamma > 60$ MeV, which as discussed is solely dominated by the direct hard-photon component. In contrast, no anisotropy is found in the angular distribution of photons in the energy region $E_\gamma = 30$-40 MeV. In this range the presence of thermal photons, emitted isotropically in secondary NNγ collisions, could be high enough to blur the small anisotropy of the prompt bremsstrahlung component emitted in first-chance collisions. Thus, these slightly different α values could be interpreted as an indication of the distinct origins of the two hard-photon contributions measured in this low energy range. However, we have to remark the relative large errors associated

with the measured α's.

6.2.2 Double source analysis of the full ($E_\gamma > 30$ MeV) hard-photon angular distribution

Taking into account the results obtained from the fits of the hard-photon angular distributions measured in the lower energy region and that of $E_\gamma > 60$ MeV, we have fitted the total ($E_\gamma > 30$ MeV) laboratory hard-photon angular distribution with the following expression:

$$\left(\frac{dN}{d\Omega}\right)_{lab} = \frac{K^d}{(Z^d)^2}\left[1-\alpha+\alpha\,\frac{\sin^2\theta_\gamma^{lab}}{(Z^d)^2}\right] E_0^d\, e^{-30\,Z^d/E_0^d} + \frac{K^t}{(Z^t)^2}\,E_0^t\, e^{-30\,Z^t/E_0^t} \qquad (6.6)$$

where $Z^d = \gamma_d(1-\beta_S^d\cos\theta_{lab})$ and $Z^t = \gamma_t(1-\beta_S^t\cos\theta_{lab})$. The first term of the equation represents the dominant contribution of the direct hard-photon emission, with the experimental inverse slope E_0^d and the normalization K^d parameter. The second term accounts for the photon emission from a secondary and thus isotropic bremsstrahlung source with the associated experimental parameters E_0^t and K^t. Table 6.6 reports the

β_S^d	β_S^t	α	$I_t/I_{tot}(\%)$	χ^2/ndf	β_{NN}	β_{AA}
0.15 ± 0.01	0.16 ± 0.01	0.0 ± 0.1	26% ± 2%	1.5	0.157	0.164

Table 6.6: *The direct and thermal source velocities and the ratio of thermal to total intensities obtained from the fit of Eq. 6.6 to the total ($E_\gamma > 30$ MeV) laboratory angular distribution. The values of the nucleon-nucleon and nucleus-nucleus velocities are also reported.*

parameters extracted from such a fit. These measured values for the direct and thermal source velocities are compatible with the expected one $\beta_{NN} \approx \beta_{AA}$. The value of the ratio I_t/I_{tot} is roughly equal to that measured in the hard-photon energy spectrum. Therefore, we can conclude that the double source fit consisting of an anisotropic plus an isotropic angular term is capable of reproducing the experimental full ($E_\gamma > 30$ MeV) inclusive angular distribution of hard photons emitted in the $^{129}\mathrm{Xe} + ^{nat}\mathrm{Sn}$ reaction at 50A MeV.

However, the measured value for the dipole strength of the direct component is equal to zero, unlike the strength of the dipole component of the angular distribution of photons above 60 MeV. Besides the fact that photons of $E_\gamma > 60$ MeV have a little weight ($\sim$ 12%) in the hard-photon inclusive spectrum, the zero anisotropy value can be related, on

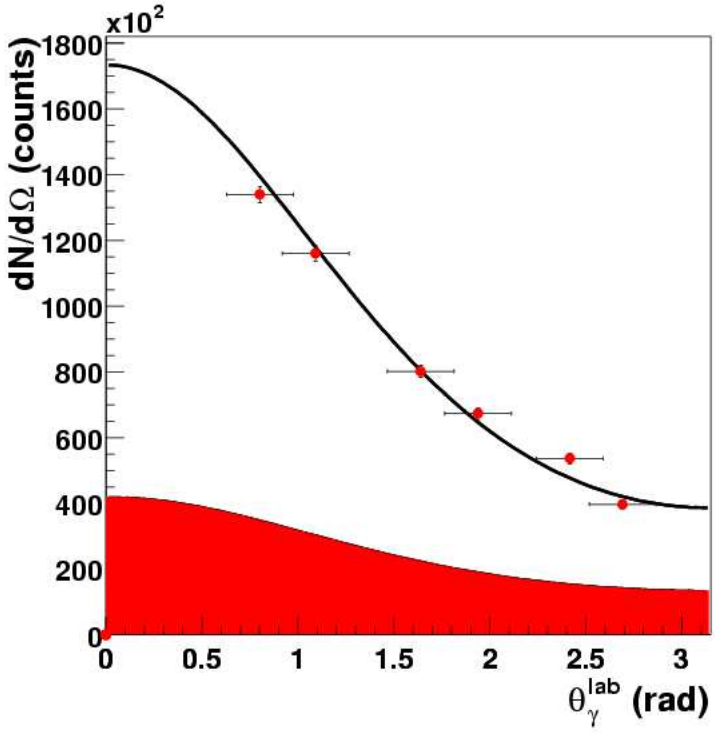

Figure 6.10: *Experimental angular distribution measured in the laboratory frame for hard-photons ($E_\gamma > 30$ MeV). The solid line represents a fit of Eq. 6.6. The dark region is an estimation of the thermal hard-photon contribution.*

the one side, to the fact that the ^{129}Xe + ^{nat}Sn reaction at 50A MeV is a very heavy system in which only a small anisotropy can be observed [26, 88], and on the other side, to the lack of measurements in the most forward direction. Although in the experimental set-up the position of the TAPS blocks was chosen in order to optimize the detection of photons emitted in the forward directions, we have to point out that there is an uncovered forward angular region ($\theta_{lab} < 32°$) due to the presence of the Forward Wall.

6.3 Charged particle distributions

In this section the inclusive charged particle distributions measured in the Dwarf Ball and in the Forward Wall are presented and compared. Since in an inclusive measurement no reaction class selection is done, a minimum bias (MB) reaction trigger, whose probability to be fired does not depend in principle on the type of event, is used. In the present experiment the "DB or ds (down scaled)" trigger, defined by the condition of detecting only a charged particle in the Dwarf Ball, worked as the MB reaction trigger.

6.3.1 Charged particle multiplicities measured in the Dwarf Ball

Fig. 6.11 depicts the total charged particle distribution measured in the Dwarf Ball, M_{CP}^{DB}. One can note that the highest cross-sections correspond to the lowest multiplicities, $M_{CP}^{DB} = 1\text{-}2$. This low charged particle multiplicity region is due, as it can be intuitively deduced and it will be discussed in chapter 7, to the most peripheral reactions. In the region of $M_{CP}^{DB} = 3\text{-}10$ the distribution exhibits a soft decreasing evolution, falling then more abruptly up to a M_{CP}^{DB} around 20. However, DB subevents with M_{CP}^{DB} above 11 exhibit a cross-section which is lower than 0.2% of the total cross section, being compatible with the estimated cross-section of random coincident events, $\sigma_{pileup} \approx P_{int} \cdot \sigma_R$, where P_{int}=1.9·10^{-3} rea./pulse. Therefore, events with a charged particle multiplicity measured in the DB higher than 11 will not be considered in the exclusive photon analysis.

In figures 6.11(b) and 6.11(c) the distributions of light-charged particles (LCP) and intermediate-mass fragments (IMF), respectively, are presented. The LCP distribution exhibits a very similar behavior with the increasing multiplicity to the shape of the total charged particle distribution in the DB. Whereas the histogram of the IMF distribution, for which the same amount of statistics as for the LCP distribution histogram has been used , presents an exponential fall off, which has also been measured in the previous KVI experiment [86]. In fact the relative cross-sections of IMF and LCP measured in the DB, $\sigma_{IMF} / \sigma_{LCP}$, amounts only to around 24%. The different LCP and IMF weight can already be estimated comparing the population of the IMF and LCP regions in Fig. 5.2.

6.3.2 Charged particle multiplicities measured in the Forward Wall

The charged particle distribution measured in the FW, see Fig. 6.12(a), exhibits with respect to the one measured in the DB, a sharper decreasing shape and above $M_{CP}^{FW} = 6$ the

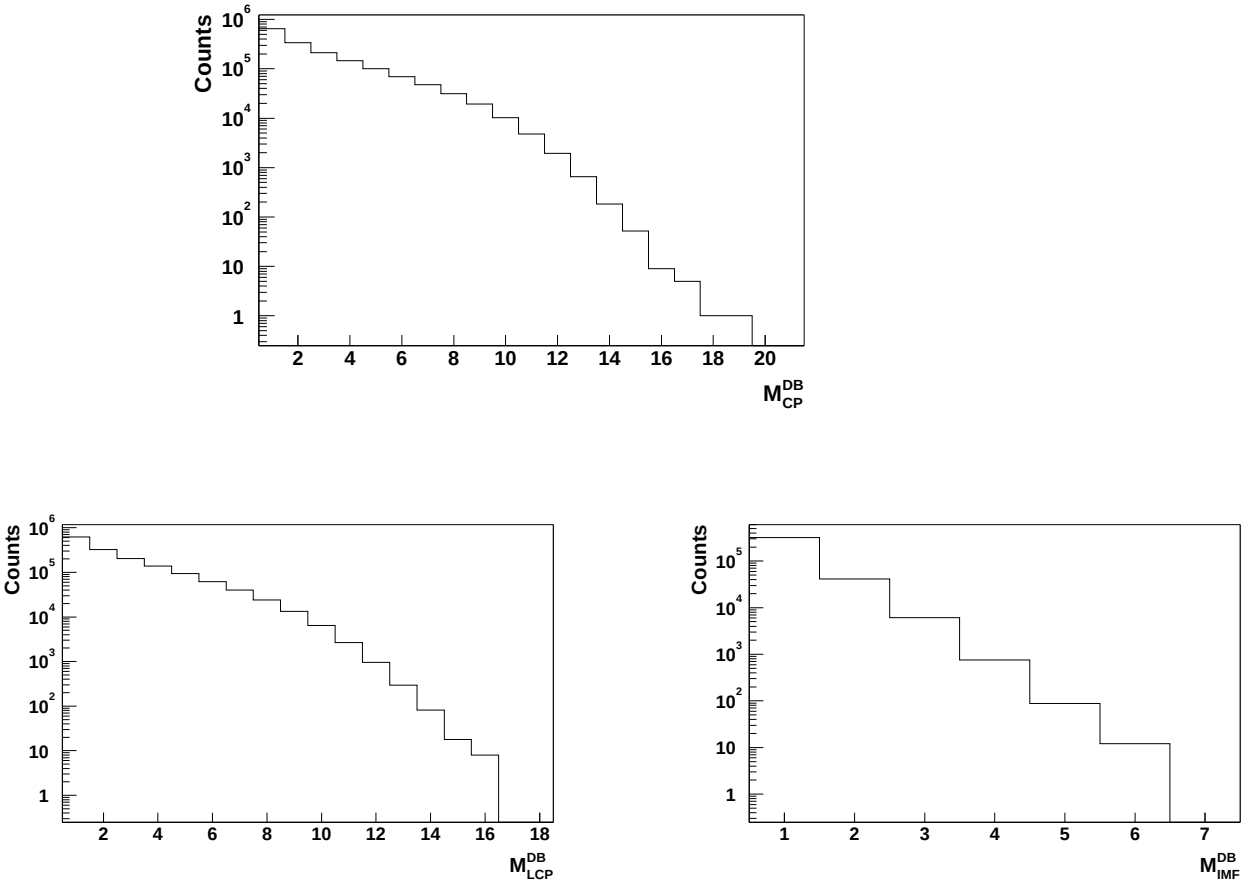

Figure 6.11: *Dwarf Ball inclusive charged particle multiplicity distributions: (a) total inclusive charged particle distribution corresponding to the total available statistics, (b) light-charged particle multiplicity distribution and (c) intermediate-mass fragment multiplicities measured both in a 12% of the available statistics.*

pileup contamination should be already important. This difference between both phoswich multidetectors is not very surprising if their distinct angular coverage, $31° \leq \theta_{DB} \leq 168°$ and $5° \leq \theta_{FW} \leq 25°$, respectively, are taken into account. When comparing the relative measured cross-sections of IMF and LCP in the DB and in the FW, in the latter case the $\sigma_{IMF}\,/\,\sigma_{LCP}$ amounts to around 48%, the double of the value measured in the DB. This higher IMF contribution, with respect to the emission of light-charged particles (see Fig. 6.13), can be understood by the higher mass of these reaction products that make the angular distibution being more forward peaked.

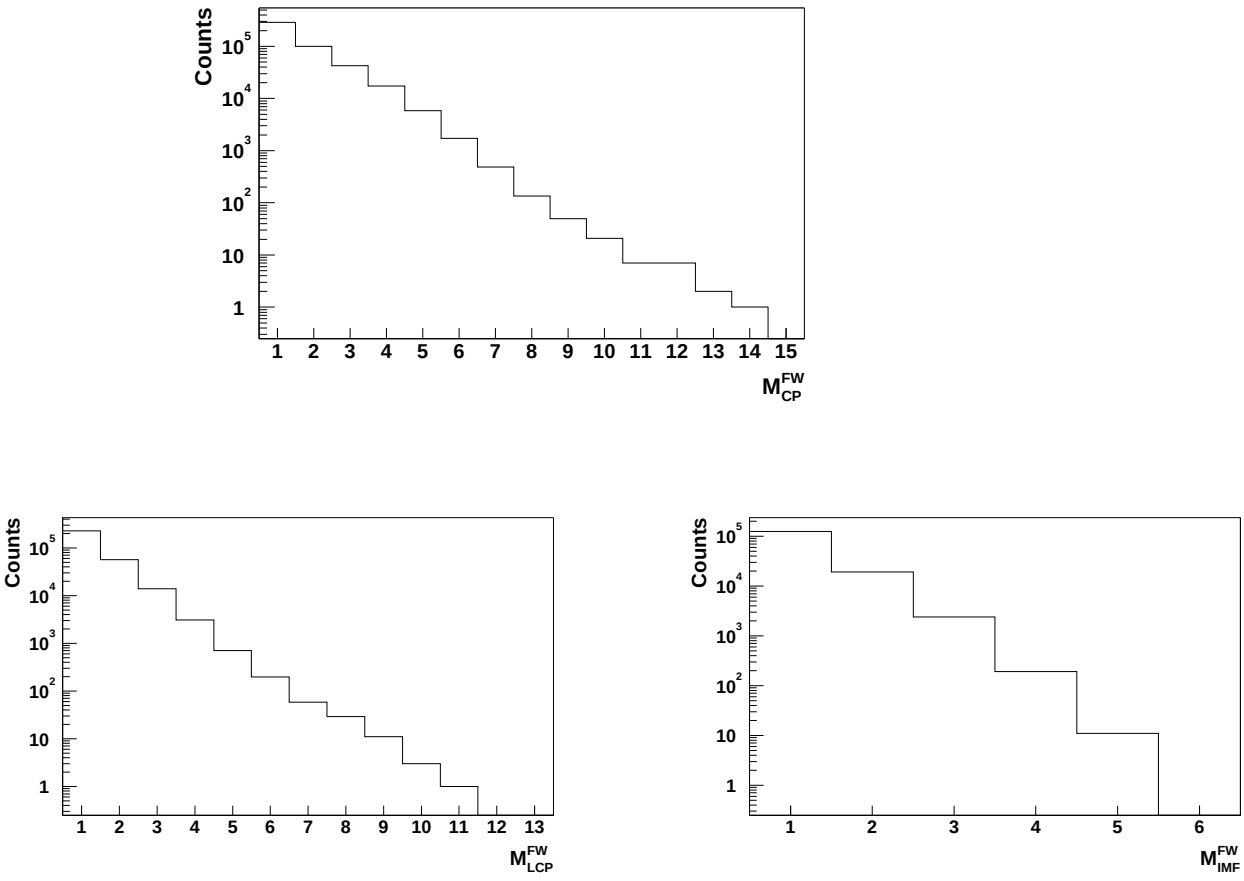

Figure 6.12: *Inclusive charged particle multiplicity distributions measured in the Forward Wall: (a) multiplicity distribution of the total charged particles and (b) distribution of the light charged particles and (c) intermediate-mass fragments. For all 3 spectra the same statistics, 12% of the total, has been used.*

6.4 Cross-sections and related measurements

6.4.1 Cross-section formula

In order to obtain the particle cross-sections our measurements have to be corrected to account for the different experimental effects.

In general, to calculate the cross section of a certain type i of reaction products N_i measured by a trigger x the following expression is used:

$$\sigma_i(\text{mb}) = C \cdot \left(\frac{SD}{T}\right)_x \cdot \frac{1}{\epsilon_x} \cdot N_i \tag{6.7}$$

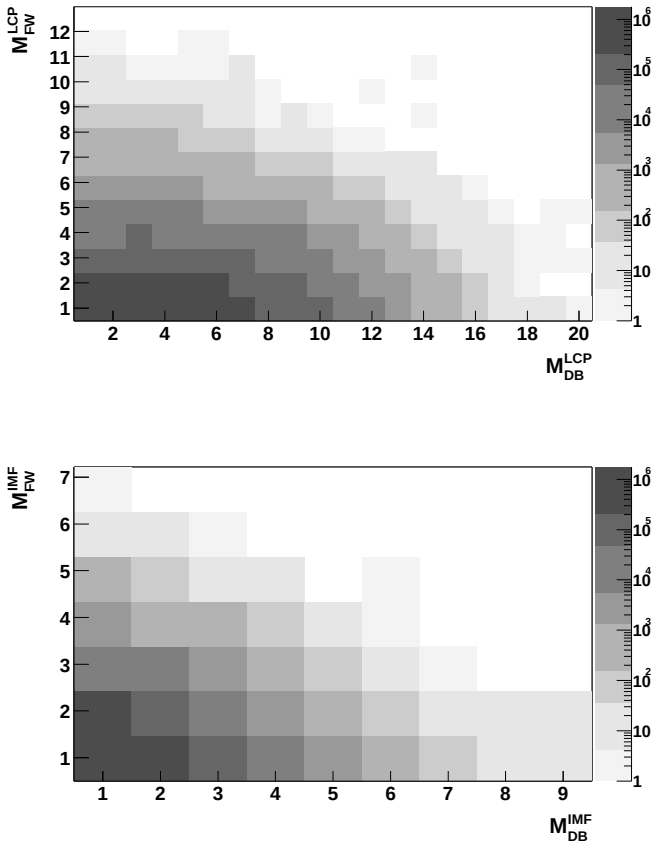

Figure 6.13: *Comparison of measured charged particle multiplicities in the Forward Wall and the Dwarf Ball: (a) LCP multiplicity detected in the Forward Wall, M^{FW}_{LCP} versus LCP multiplicity measured in the Dwarf Ball, M^{DB}_{LCP}. In (b) IMF in the FW, M^{FW}_{IMF}, as a function of the IMF multiplicity in the DB, M^{DB}_{IMF}.*

where:

- the factor C accounts for the number of projectile particles and the density of the target, and it reads as:

$$C(mb) = 10^3 \cdot \frac{A}{N_p \cdot N_A \cdot d} \tag{6.8}$$

The 10^3 factor allows to express the cross-section in millibars, N_A is Avogadro's number, d is the thickness of the Sn target expressed in mg/cm^2 and A is the atomic number of the (Sn) target. The number of projectile particles (N_p) is measured by means of the integration of the beam charge in the Faraday cup. The factor C has a relative error of around 10%. This error accounts for the statistical uncertainty

in the charge collection in the Faraday cup and the systematic error due to possible variations of the target thickness.

- The ratio between the scale down factor (SD) and the life time (T) of a trigger x is equal to the ratio between the real number of events and the number of events finally accepted by the trigger x.

- ε_x stands for the efficiency of detection of the trigger x. This factor corrects for the acceptance of the detectors and the deviations of the reaction products spectra due to the procedures used in the analysis method. The efficiency is defined as follows:

$$\varepsilon_x = \frac{N_i^M}{N_i^G} \tag{6.9}$$

Where N_i^G is the number of particles generated by means a simulation tool and N_i^M is the final number of particles measured after the analysis process.

In the case of a TAPS experiment the different particles are generated by means of a simulation package KANE [89], based on the GEANT program[81]. The output of the KANE simulation is a FOSTER ntuple with the same format as the ntuples of experimental data. The KANE ntuple is therefore used as the input of the ROSEBUD analysis, as in the experimental raw data case. The efficiency accounts then, and on the one side for the response of the detector, and on the other, for the losses introduced by the particle identification and reconstruction analyses carried out with the ROSEBUD package.

The uncertainty of the experimental cross-sections is mainly due to the errors associated to the normalization factor C and the trigger efficiency:

$$\Delta\sigma = \sigma\sqrt{\left(\frac{\Delta C}{C}\right)^2 + \left(\frac{\Delta\varepsilon}{\varepsilon}\right)^2} \tag{6.10}$$

6.4.2 Reaction cross-section

To measure the reaction cross-section we use Eq. (6.7) for the minimum bias reaction trigger, "DBor ds". To compute this trigger efficiency charged particles are generated by means of a FREESCO [90] nuclear deexitation simulation implemented in the KANE package. The estimated efficiency is $\varepsilon_R = 0.76 \pm 0.01$. The number of counts N_R is obtained by integrating the inclusive charged particle spectrum of figure 6.11(a).

The experimental reaction cross section is $\sigma_R^{exp} =$ **(5300 ± 592) mb**. This value is in good agreement with the geometrical cross-section:

$$\sigma_R^{geo}(\text{mb}) \;=\; 10 \cdot \pi \cdot R_{int}^2(\text{fm}) \cdot \left(1 - \frac{V_C(\text{MeV})}{K_{lab}(\text{MeV})}\right) \;=\; 5126 \quad \text{mb} \tag{6.11}$$

where V_C is the Coulomb barrier of Eq. (2.3) and R_{int} is the interaction radius:

$$R_{int}(\text{fm}) \;=\; 1.16 \cdot (A_t^{1/3} \;+\; A_p^{1/3}) + 2.0 \tag{6.12}$$

6.4.3 Hard photon cross sections

The experimental inclusive hard photon cross-section is obtained by computing Eq. (6.7) for the MB γ trigger ("NEUTRAL*DB"). The number of measured hard photons N_γ results from the integration of the hard photon spectrum of Fig. 6.2.

The efficiency for hard photon detection is estimated with the TAPS simulation package KANE generating a hard photon exponential distribution whose slope, related source velocity and anisotropy factor, are the measured values. The photon efficiency is calculated by dividing the number of generated photons by the number of photons finally measured. Thus the obtained efficiency $\varepsilon_{\gamma * DB} = 0.12 \pm 0.01$ accounts then, on the one side for the response of TAPS, mainly due to the geometric acceptance [73], and on the other, for the biases introduced by the reconstruction and identification of photon showers implemented within the ROSEBUD package.

The cross section of direct and thermal photons (σ_γ^d and σ_γ^t) are measured just by taking the direct and thermal experimental contributions to the total hard photon inclusive spectrum, amounting to (78 ± 1) % and (22 ± 1) %, respectively. The total, direct and thermal cross sections are listed in Table 6.7.

6.4.4 Hard photon multiplicities

The main source of uncertainty of the former hard photon cross-sections comes from the error associated with the cross section normalization factor C. It is therefore advantageous to determine the experimental *direct* and *thermal hard photon multiplicities*, which are related to the direct and thermal cross-sections but do not rely on the C factor. The direct (thermal) hard photon multiplicity, i.e. the number of direct (thermal) hard photons emitted per nuclear reaction, is deduced from the following expression:

$$M_\gamma^i \;=\; \frac{\sigma_\gamma^i}{\sigma_R} \quad \text{with i = direct, thermal} \tag{6.13}$$

where σ_R is the experimental reaction cross section (see Section 6.4.2). We report the obtained direct and thermal hard photon multiplicities in Table 6.7.

6.4.5 Hard photon probability

The direct hard photon probability P_γ^d, i.e. the probability to produce a hard photon in a first chance pn collision, is determined from the experimental direct hard photon multiplicity:

$$P_\gamma^d = \frac{\sigma_\gamma^d}{\sigma_R \cdot \langle N_{pn} \rangle_b} = \frac{M_\gamma^d}{\langle N_{pn} \rangle_b} \tag{6.14}$$

where $\langle N_{pn} \rangle_b$ is the number of first chance pn collisions averaged over impact parameter calculated from the geometrical model (see 2.8). $\langle N_{pn} \rangle_b$ is equal to 11.79 for the Xe on Sn system. The measured P_γ^d is reported in Table 6.7. We note that we do not quote a thermal hard photon probability, since we should determine the average number of secondary (and not primary) pn collisions, from which the thermal component originates, is not well determined experimentally nor theoretically.

However as we will discuss in the next section, the empirical Eq. (2.10) is obtained from the experimental systematics of hard photon production and refers to a total (direct + thermal) hard photon probability, P_γ^{sys}. Thus, in order to compare our inclusive hard photon results with the systematics we have calculated this total hard photon probability, taking the total (direct + thermal) hard photon multiplicity and $\langle N_{pn} \rangle_b$. The experimental P_γ (reported in Table 6.7) is in good agreement with the value predicted from the systematics, $P_\gamma^{sys} = 0.98 \cdot 10^{-4}$.

6.5 New direct hard photon systematics

The empirical exponential expressions describing the correlation between the bombarding energy and the experimental hard photon inverse slope parameters and probabilities [Eq. (2.4) and Eq. (2.10), respectively] were deduced from the systematics collected since the first (hard) photon experiments in 1985 [27, 28, 29, 30]. However, only from the TAPS experimental campaign of 1992 the photon double source fit of the spectra allowed to distinguish and to isolate the first chance (direct) NN bremsstrahlung radiation from the thermal NN bremsstrahlung component. Therefore, the original formulas do not describe the relation of the direct hard photon emission with the bombarding energy but of a mixed systematics consisted of total and direct slopes and probabilities.

Reaction properties ^{129}Xe + ^{nat}Sn at 50A MeV			
K_{Cc} (MeV)	47.8		
E_{Cc}^{AA}(MeV)	11.2		
β_{NN}	0.157		
β_{AA}	0.164		
$\langle N_{pn} \rangle_b$	11.79		
Inclusive hard γ results			
	Total	Direct	Thermal
E_0(MeV)	-	15.6 ± 1.0	7.0 ± 0.6
β	-	0.15 ± 0.01	0.16 ± 0.01
σ_γ(mb)	6.25 ± 0.73	4.88 ± 0.57	1.37 ± 0.17
M_γ	(1.18 ± 0.11)·10^{-3}	(9.24 ± 0.82)·10^{-4}	(2.61 ± 0.27)·10^{-4}
P_γ	(1.00± 0.07) ·10^{-4}	(7.83 ± 0.70) · 10^{-5}	-

Table 6.7: *Main reaction characteristics and summary of the experimental inclusive hard photon results for the $^{129}Xe + ^{nat}Sn$ reaction at 50A MeV.*

Table 6.8 reports the HI reactions studied since 1992 where a double source hard photon analysis has been performed: the 8 different reactions studied by the TAPS collaboration [40, 26] (including the one investigated here), and the three different Ni induced reactions at 30A MeV studied by the MEDEA collaboration [91]. By compiling the direct hard photon results obtained in these analyses we can try to describe the systematic dependence of the **direct** hard photon slope and production probability on the Coulomb corrected (Cc) bombarding energy.

6.5.1 Direct hard photon slope

The evolution of the direct hard photon slope as a function of the Cc bombarding energy (K_{Cc}) is presented in Fig. 6.14. One can note comparing this Figure and Fig. 2.2, that the direct and the total hard photon experimental slopes exhibit a very similar dependence on K_{Cc}. Thus, the following function is deduced from the E_0^d systematics:

$$E_0^d = a\,(K_{Cc})^b \tag{6.15}$$

with $a = 0.53 \pm 0.08$ and $b = 0.90 \pm 0.04$. This relation is equal to the one of the total bremsstrahlung slope systematics of Eq. 2.4 except for a light change in the fitting

Reaction	E_0^d (MeV)	E_0^t (MeV)	$I_t/I_{tot}(\%)$	$M_\gamma^d(10^{-4})$	$P_\gamma^d(10^{-5})$	$M_\gamma^t(\cdot 10^{-4})$
^{86}Kr+^{58}Ni at 60A MeV [40]	20.2 ± 0.4	8.5 ± 0.8	25.0 ± 1.0	6.0 ± 1.2	8.6 ± 0.9	2.0 ± 0.2
^{181}Ta+^{197}Au at 40A MeV [40]	13.4 ± 0.8	6.9 ± 0.6	33.0 ± 1.0	9.6 ± 2.0	3.6 ± 0.3	3.2 ± 0.3
^{208}Pb+^{197}Au at 30A MeV [40]	10.1 ± 0.4	5.5 ± 0.6	38.0 ± 1.0	1.0 ± 3.2	0.5 ± 0.0	0.6 ± 0.2
^{36}Ar+^{197}Au at 60A MeV [42]	20.1 ± 1.2	6.8 ± 0.6	18.5 ± 1.0	7.0 ± 0.7	10.0 ± 1.6	1.6 ± 0.2
^{36}Ar+^{107}Ag at 60A MeV [42]	20.1 ± 1.3	7.0± 1.0	16.0 ± 2.0	6.6 ± 0.2	11.7 ± 1.8	1.2 ± 0.2
^{36}Ar+^{58}Ni at 60A MeV [42]	20.9 ± 1.3	6.9 ± 0.8	19.5 ± 1.0	4.4 ± 0.2	9.8 ± 1.4	1.1 ± 0.2
^{36}Ar+^{12}C at 60A MeV [42]	18.1 ± 1.1	0.0 ± 0.5	0.0 ± 5.0	1.9 ± 0.3	10.1 ± 3.2	0.0 ± 0.6
^{129}Xe+^{112}Sn at 50A MeV	15.6 ± 1.0	7.0 ± 0.6	22.0 ± 1.0	9.2 ± 0.6	7.8 ± 0.6	2.6 ± 0.2
^{58}Ni+^{27}Al at 30A MeV [91]	10.3 ± 0.5	4.8 ± 0.2	20.0 ± 5.6	-	-	-
^{58}Ni+^{58}Ni at 30A MeV [91]	10.2 ± 0.5	5.2 ± 0.4	37.5 ± 12.5	-	-	-
^{58}Ni+^{197}Au at 30A MeV [91]	12.4 ± 0.7	4.3 ± 0.2	41.1 ± 11.7	-	-	-

Table 6.8: *Parameters characterizing the inclusive hard photon production for the HI reactions where a double source hard photon analysis has been performed. For each reaction we report the measured direct (E_0^d) and thermal (E_0^t) hard photon slopes, the ratio of thermal to total bremsstrahlung yield (I_t/I_{tot}), the direct multiplicity (M_γ^d) and probability (P_γ^d), and the thermal multiplicity (M_γ^d).*

parameters ($a = 0.48 \pm 0.06$ and $b = 0.91 \pm 0.03$).

6.5.2 Direct hard photon production probability

The direct hard photon production probability systematics as a function of the Cc bombarding energy is presented in Figure 6.15. The expression deduced from the total hard photon probability systematics, Eq.(2.10) (dashed line in Fig.6.15), does not describe properly the experimental direct hard photon probability at the lowest bombarding energy, for which the ratio of thermal to total hard photon yield is the highest. However, the experimental direct hard photon production probability systematics exhibits an exponential dependence on the bombarding energy, as the total hard photon probability systematics does. This dependence can be parameterized in the P_γ^d case through the E_0^d by the function (solid line in Fig.6.15):

$$P_\gamma^d = P_0^d \, e^{-30(MeV)/a \cdot K_{Cc}} \tag{6.16}$$

with $P_0^d = (1.21 \pm 0.19) \cdot 10^{-3}$ and $a = 0.22 \pm 0.01$. By comparing this expression with the one deduced from the total hard photon probability systematics, Eq. (2.10), we can conclude that the change in considering the E_γ^d and P_γ^d systematics, instead of the total

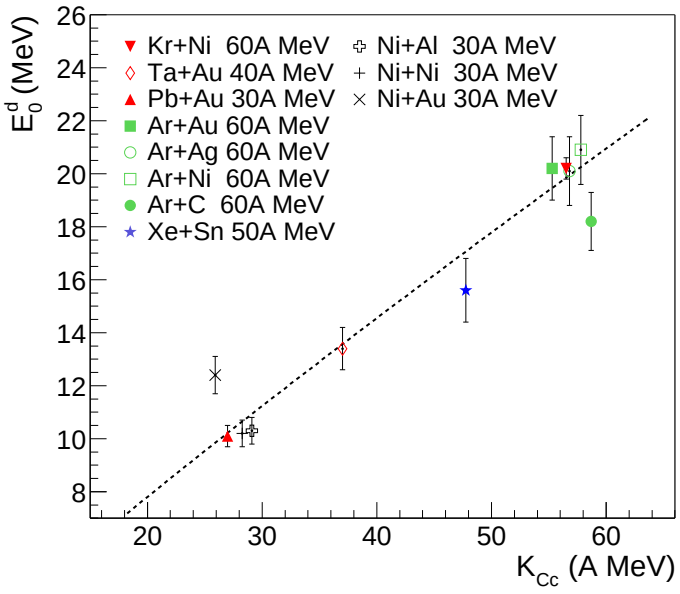

Figure 6.14: *Systematics of direct hard photon slope, E_0^d, as a function of the Cc bombarding energy K_{Cc}. The measurements correspond to different TAPS reactions [25, 26] and to three Ni induced reactions studied by MEDEA [91]. The dashed line is the fit of Eq. 2.4 to the data.*

hard γ slope and probability systematics, is not reflected in a radical change of the type of dependence on the K_{Cc}, but in the strength of this dependence. This result confirms that the first chance bremsstrahlung emission constitutes the dominant component of the total hard photon spectrum and hence the direct and total slopes are expected to follow a very similar trend with the bombarding energy.

6.6 Thermal hard photon systematics

As in the former section we consider here the experiments where a thermal hard photon component has been measured (Table 6.8) to investigate the systematics of the thermal bremsstrahlung emission.

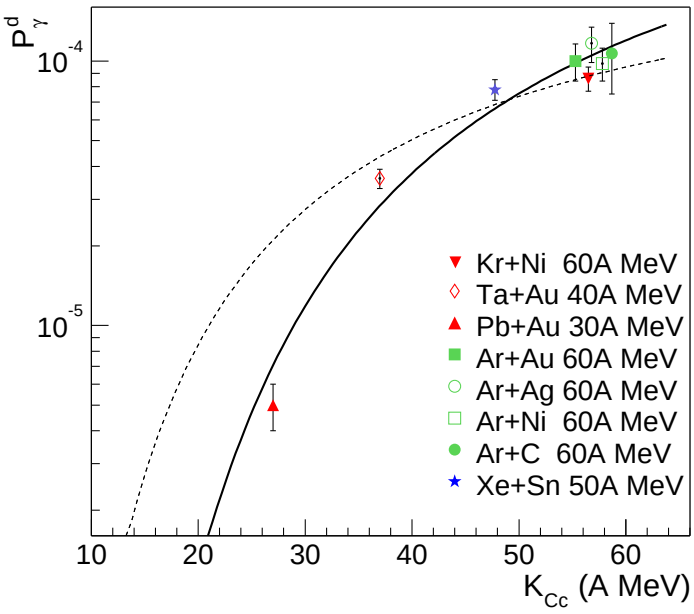

Figure 6.15: *Compilation of direct hard photon probabilities P_0^d plotted as a function of the Cc bombarding energy K_{Cc}. The experimental points correspond to the different TAPS direct hard photon measurements. The dashed line represents a fit to Eq. (2.10) obtained from the total hard photon systematics. The solid line is a fit to Eq. (6.16).*

6.6.1 Thermal hard photon slope

In Figure 6.16 the compilation of thermal slopes (Table 6.8) plotted as a function of the Cc available energy in the nucleus-nucleus center of mass, $E_{Cc}^{AA} = A_{red} K_{Cc}^{lab}/A_{tot}$, is presented. The Figure has been adapted from [42] by adding the thermal slopes reported in [91].

The experimental thermal slope measured in the ^{129}Xe + ^{nat}Sn at 50A MeV reaction follows the linear dependence on the Cc available energy in the nucleus-nucleus center of mass, E_{Cc}^{AA} discussed in 2.3.1. In order to evidence the different origin of the thermal and direct bremsstrahlung components we have plotted in Fig. 6.17 the compilation of measured thermal slopes as a function of the K_{Cc}^{lab} (left panel) and the E_0^d systematics as a function of the E_{Cc}^{AA} (right panel). Taking only into account the thermal and direct slopes corresponding to the asymmetrical systems, one can check that on the one side, thermal slopes do not scale with the bombarding energy and on the other, direct slopes

do not exhibit, as the thermal ones do, a linear dependence on the available energy in the nucleus-nucleus center of mass. This result is consistent with a thermal origin of the second bremsstrahlung emission [26, 42].

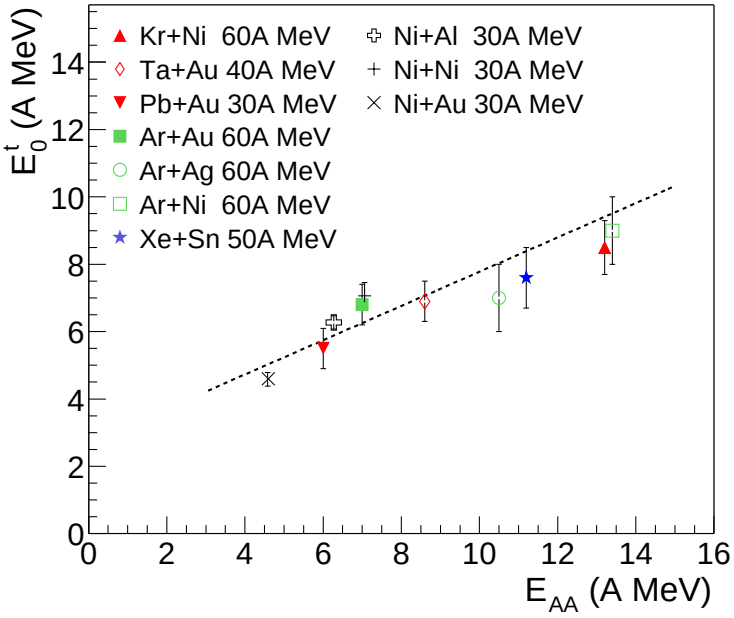

Figure 6.16: *Compilation of thermal hard-photon slopes E_0^t, measured at $\theta_\gamma^{lab} = 90°$, plotted as a function of the corrected nucleus-nucleus center-of-mass energy E_{Cc}^{AA}. The solid line is a linear fit to the data.*

6.6.2 Thermal hard photon multiplicity

As discussed in 6.4.5, a thermal hard photon probability systematics is not available. However, we can exploit what we have learned about the thermal slope and the direct probability systematics to discuss the available systematics of the thermal hard photon multiplicity. On the one side, in analogy with the expression of the direct photon multiplicity of Eq. (6.13), the thermal hard γ multiplicity is equal to the product of an unknown thermal hard photon probability times the number of second chance pn collisions, which should scale with the system size ($A_{tot} \approx A_1 + A_2$). On the other side, and also in analogy with the direct hard photon dependence on the bombarding energy, the thermal probability is expected to scale with the available energy in the nucleus-nucleus

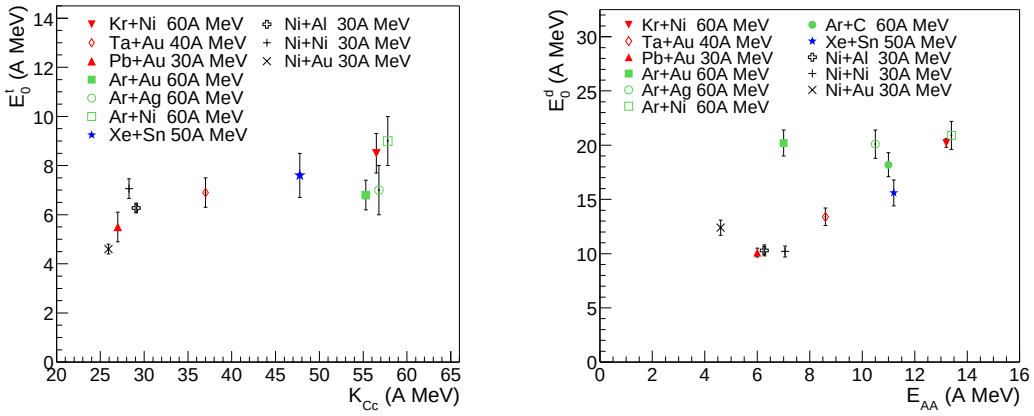

Figure 6.17: *Left panel: systematics of thermal hard photon slopes as a function of the (Coulomb corrected) bombarding energy. Right panel: direct hard photon slopes plotted as a function of the Cc nucleus-nucleus center-of-mass energy.*

center of mass. Therefore the thermal hard photon multiplicity normalized to the size of the system should exhibit a linear dependence on the available energy in the nucleus-nucleus center of mass. As a matter of fact, this is indeed the behavior observed in Fig.6.18 which plots the systematics of the thermal hard photon multiplicity as a function of the Coulomb corrected available energy in the nucleus-nucleus center of mass.

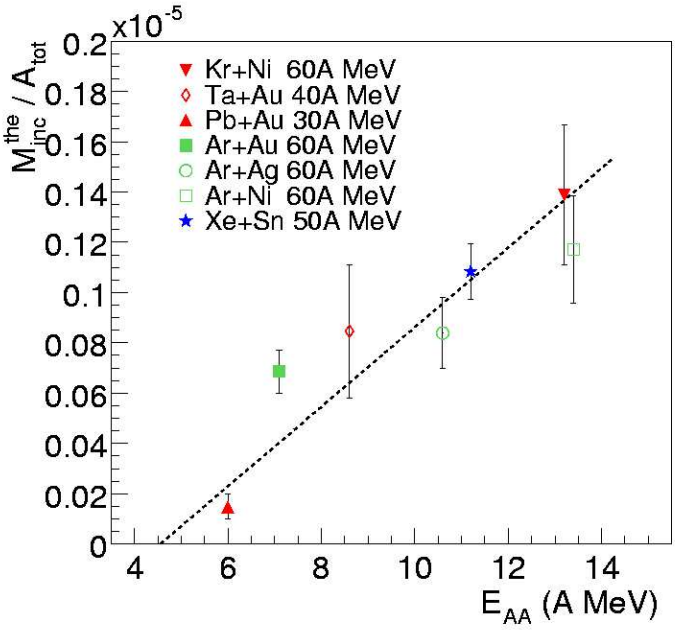

Figure 6.18: *Systematics of inclusive thermal hard photon multiplicity normalized by the system size ($A_{tot} \approx A_1 + A_2$) as a function of the Cc available energy in the nucleus-nucleus center-of-mass. The measurements correspond to the different TAPS experiments.*

Chapter 7

Exclusive hard photon analysis

The exclusive analysis of the dependence of the thermal hard photon emission on the centrality of the collision is of great interest. The path followed by the system formed during the reaction, along the nuclear phase diagram depends on the reached excitation energy, and hence on the impact parameter of the reaction.

In this chapter the exclusive hard photon analysis performed for ^{129}Xe + ^{nat}Sn reactions at 50A MeV is reported. A global exclusive measurement on the behavior of the photon production with the centrality is presented in the first section. Then we will focus on more selective measurements which have been carried out for the first time in the present experiment. The method employed to measure the impact parameter for a given reaction centrality class is described in the second section. The characteristics of the reaction classes selected for the exclusive hard photon analysis are presented in section 7.3. In the next section the results on the thermal hard photon production as a function of the impact parameter are presented. In the last section I present the investigation on the γ yield from the Giant Dipole Resonance (GDR) decay, which has been undertaken to detect any possible GDR contribution to the photon spectrum above 30 MeV.

7.1 Gross exclusive measurements

The detected charge particle multiplicity is an indicator of the violence of HI collisions. Reactions associated to small (large) impact parameter reactions are related with a high (low) production of particles. This aspect is evinced when particle yields are plotted as a function of the charged particle multiplicity. So, as a first step of our exclusive hard photon analysis, we have investigated the evolution of the photon yield along all the

range of charged particle multiplicities measured in the Dwarf Ball. We have considered 3 different energy regions:

- Photons of 10 MeV < E_γ < 22 MeV, which are expected to come mainly from the decay of Giant-Dipole Resonances;
- The region of 30 MeV < E_γ < 45 MeV consisted, as discussed in 6.1.2, of a mixed contribution of thermal and direct photons;
- Photons above 60 MeV, that should only come from direct production.

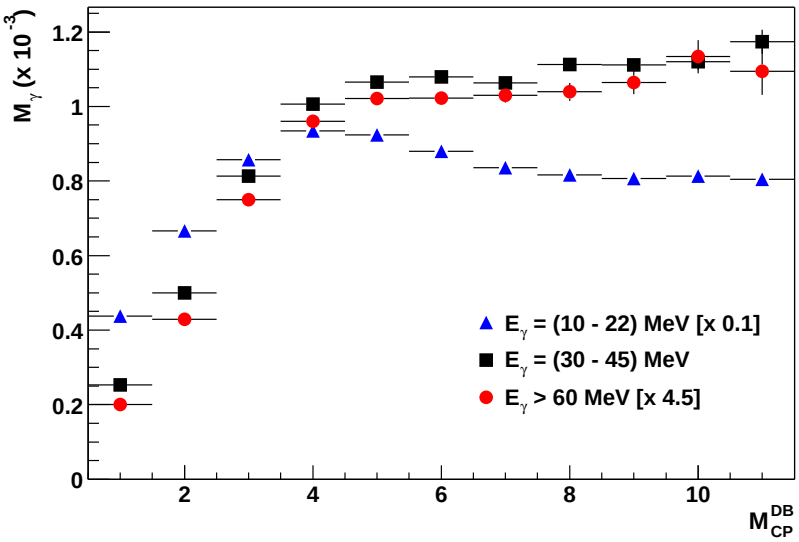

Figure 7.1: *Photon multiplicity, M_γ, as a function of the charged particle multiplicity measured in the DB, M_{CP}^{DB}.*

One can observe in the Figure 7.1 that whereas both hard photon components exhibit the same increasing behavior with the charged particle multiplicity, low energy photons show a maximum at M_{CP}^{DB}=4 followed by a saturation, which is compatible with the GDR quenching measured at high excitation energies $\epsilon^\star > 3$ MeV [92]. The suppression of the GDR has been proposed as a signal of the liquid-gas phase transition [24, 93].

The $M_\gamma(M_{CP}^{DB})$ measurement has been also motivated to compare our result with the one observed for the ^{36}Ar+^{197}Au at 60A MeV reaction studied at the KVI laboratory [42]. The dependence on M_{CP}^{DB} of both hard photon energy ranges (25 MeV < E_γ < 35 MeV and E_γ > 50 MeV) measured for that system are similar and compatible with the

behavior observed for the hard photon energy ranges measured in the Xe+Sn reaction. The decrease with the increasing centrality of the low energy γ component (10 MeV $<$ E_γ $<$ 18 MeV) measured for the ^{36}Ar+^{197}Au reaction is even stronger, by a factor 2 between the maximum photon multiplicity and the M_γ at the highest M_{CP}^{DB}.

These gross measurements suggest that both (direct and thermal) hard photon yields might not exhibit very different behaviors compared to the centrality dependence of GDR photons. However, to address the question of the dependence of the thermal hard photon production, and thus of thermal equilibration, on impact parameter, an exhaustive analysis is clearly needed:

1. The centrality has to be quantitatively estimated in order to express the hard photon production as a function of impact parameter.

2. The hard γ spectrum has to be analyzed from peripheral to central collisions, to extract the dependence of the thermal hard photon slope and yield on the impact parameter.

The high hard photon statistics of the present experiment in concomitance with a complete charged-particle set-up have enabled to undertake for the first time such an exclusive investigation.

7.2 Estimation of the impact parameter

7.2.1 Impact parameter estimation from the charged particle multiplicity

The impact parameter b can be deduced in nucleus-nucleus collisions from the experimental charged particle yield M_{CP} by means of the geometrical method proposed by Cavata *et al.* [94]. This method assumes that:

1. The reaction cross-section is well approximated by the geometrical cross-section,

$$\sigma_R(mb) \approx 10\,\pi\, b_{max}^2 \tag{7.1}$$

where

$$b_{max}(fm) = r_0 \cdot (A_p^{\frac{1}{3}} + A_t^{\frac{1}{3}}) \quad \text{with } r_0 \approx 1.2 \tag{7.2}$$

2. The charged particle multiplicity M_{CP} decreases monotonously as a function of the impact parameter.

Thus, the difference between the total reaction cross-section and the one of reactions with a given impact parameter b reads as:

$$\sigma_{b_{max}-b} = \pi\,(b^2_{max} - b^2) = \int_{M'_{cp}=1}^{M^{max}_{cp}} \frac{d\sigma(M'_{cp})}{dM'_{cp}}\,dM'_{cp} - \int_{M_{cp}(b)}^{M^{max}_{cp}} \frac{d\sigma(M'_{cp})}{dM'_{cp}}\,dM'_{cp}$$
$$= \sum_{M'_{cp}=1}^{M'_{cp}=M_{cp}(b)} \sigma(M'_{cp}) \tag{7.3}$$

From Eq. (7.3) the impact parameter can be estimated as:

$$b = \sqrt{b^2_{max} - \frac{1}{\pi}\sum_{M'_{cp}=1}^{M'_{cp}=M_{cp}} \sigma(M'_{cp})} = b_{max}\sqrt{\frac{1}{\sigma_R}\sum_{M'_{cp}=M_{cp}}^{M'_{cp}=M^{max}_{cp}} \sigma(M'_{cp})} \tag{7.4}$$

7.2.2 Impact parameter estimation from the direct hard photon yield

An alternative (although less straightforward) method to deduce the impact parameter in experiments where the hard photon emission can be analyzed is based on the correlation of the direct hard γ multiplicity with the impact parameter, relying on the equal-participant geometrical model of Nifenecker and Bondorf [36].

Intuitively, knowing that the inclusive direct hard γ multiplicity, as discussed in the former chapter, is proportional to the number of first chance pn collisions, one can expect that the hard γ multiplicity increases with the projectile and target degree of overlapping, i.e. with the centrality. And in fact, this has been extensively observed in several exclusive studies on hard photon production (see e.g. [95, 96, 97, 83, 92, 98]). Direct hard photons are therefore exploited in our analysis as probes to measure the reaction impact parameter.

Due to the low probability of producing a bremsstrahlung photon in a pn collision, the reaction centrality cannot be selected by means of direct hard photons on an event-by-event basis. The impact parameter selection is hence performed in two steps:

1. Reaction classes are selected by imposing different conditions on charged-particle observables sensitive to the reaction centrality.

2. The average impact parameter of each reaction class is deduced from the measured direct hard photon multiplicity.

The charged particle observables depending on centrality that are exploited in the first step are mainly: the total charged particle [99, 26] and the LCP [96, 40] multiplicities, the size and velocity of the projectile-like fragments (PLF) [40, 92] and, as presented in a recent work [98], the ratio of the residue velocity to the center of mass velocity. The PLF method is restricted however to binary reactions, and hence, to rather large impact parameter classes. We have to point out that these are not the only impact parameter indicators but the ones typically exploited in exclusive hard photon investigations [1].

In the present work, as the ultimate goal was to study the hard photon emission from peripheral to central collisions, and considering the characteristics of charged particle detectors, the charged particle multiplicity has been adopted naturally as the event centrality selector.

From the direct hard photon multiplicity $M_\gamma^d(RC)$ measured in a given reaction class RC, and from the direct hard photon probability P_γ^d (see 6.4.5), which is considered to depend only on the (Coulomb corrected) bombarding energy, the experimental average number of first chance pn collisions $\langle N_{pn}(RC)\rangle$ reads as:

$$\langle N_{pn}(RC)\rangle \;=\; \frac{M_\gamma^d(RC)}{P_\gamma^d} \tag{7.5}$$

According to the equal-participant geometrical model [36], by modifying Eq. (2.8), the average number of first chance pn collisions for a given impact parameter can be written as:

$$N_{pn}(b) \;=\; A_{part}(b)\cdot\left(\frac{Z_pN_t + Z_tN_p}{A_p\,A_t}\right) \quad \text{assuming } A_p \le A_t \tag{7.6}$$

where A_p, Z_p, N_p, A_t, Z_t, N_t are the mass, charge and neutron numbers of the projectile and target respectively. $A_{part}(b)$ reads as:

$$A_{part} \;=\; \frac{5}{4}\,A_p(2 \;-\; 3\cos\theta_p \;+\; \cos^3\theta_p) \;+\; \frac{1}{4}\,A_t(2 \;-\; 3\cos\theta_t \;+\; \cos^3\theta_t) \tag{7.7}$$

with

$$\cos\theta_{p,t} \;=\; \frac{b^2 + R_{p,t}^2 - R_{t,p}^2}{2\,b\,R_{p,t}^2} \quad \text{and } R_{p,t} \;=\; 1.15\,A_{p,t}^{1/3} \tag{7.8}$$

The average impact parameter of each reaction class is hence deduced from expression (7.6) and from the measured $\langle N_{pn}(RC)\rangle$ values (see solid line of Figure 7.3). We note that if the impact parameter is obtained directly from the total hard photon yield, as commonly done, instead of only from the direct component, the deduced impact parameter might be distorted for reactions where a thermal photon contribution cannot be neglected.

[1] A detailed study of the charged particle observables sensitive to the reaction centrality and their correlation for the Xe+Sn at 50A MeV reaction can be found in [100, 43, 101].

7.3 Selection of reaction classes

Among different candidates, 6 reaction classes have been selected to investigate the dependence of the thermal hard photon production on centrality. This choice results from a compromise between requiring a global wide impact parameter coverage and obtaining enough statistics in hard photon production for each reaction class. We report in Table 7.1 the conditions on the charged particle multiplicities measured in the SSD, Dwarf Ball and Forward Wall that define the selected reaction classes A through F(see also Fig. 7.2). Since, as discussed in section 5.4.1, the SSD multiplicity values are restricted to one and zero, when we consider here the total charged particle multiplicity M_{CP}^{TOT}, we refer mainly to the sum of the multiplicity measured in the DB and the FW.

Why have we chosen a *total* charged particle multiplicity criterion instead of applying different correlations between the multiplicity of fragments measured in the 3 detectors, and the multiplicity of LCP measured in both phoswich multidetectors? The reason is that the total accumulated hard photon statistics measured in reaction classes selected by alternative and more exclusive criteria are too low (less than 10^4 photons) to perform a safe double hard γ source analysis. For instance, reactions where at least 3 intermediate-mass fragments are measured in the DB account only for 2% of the total cross section. So, with the available statistics, a reaction selection based on IMF multiplicity conditions becomes impossible if one intends to investigate the thermal hard photon emission in an exclusive manner.

Comparing the criteria imposed to classify events as reaction class A or B (see Table 7.1), reaction class A is indeed a subgroup of class B for which an additional condition on the SSD multiplicity is required. Such a condition has been imposed after investigating the correlation of the hard photon multiplicity and the SSD measurements. The hard photon multiplicity is found to be slightly higher, reflecting a larger impact parameter, when a fragment is measured in the SSD at polar angles lower than 5°. So, the opposite case ("M^{SSD} (at $\theta < 5°$) = 0") is required to tag the most peripheral case, reaction class A. However, at this point we have to note that the largest impact parameter reactions are almost inaccessible in our exclusive hard photon measurements. In peripheral collisions, on the one side the number of pnγ collisions is lower than in central ones, and on the other, the extra Fermi nucleon momentum, necessary to produce a hard photon in a pn collision, is less important in the surface of the nucleus than in its central part. Therefore, the selection of nuclear reactions for which a hard photon is measured implies an intrinsic bias

toward low impact parameter reactions. As a matter of fact, the requirement of the MB photon trigger (a photon of $E_\gamma > 10$ MeV in coincidence with a charged particle detected in the DB), already biases the accepted event centrality toward low impact parameters. This effect can be appreciated by comparing the contribution of each reaction class to the total reaction cross section, σ_R, and to the partial reaction cross section involving the MB γ trigger, $\sigma_R(\gamma$*DB), reported in Table 7.1.

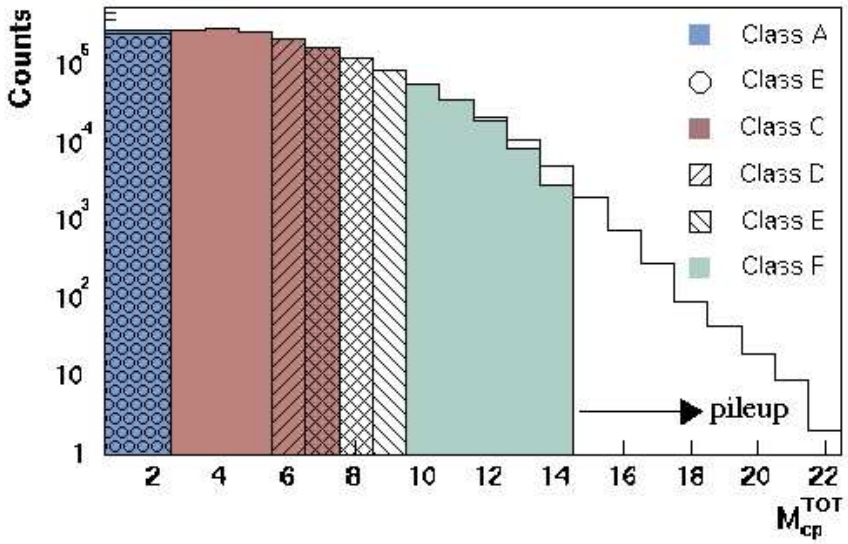

Figure 7.2: *Total charged particle distribution* $M_{CP}^{TOT} = M_{CP}^{DB} + M_{CP}^{FW}$ *of each selected reaction class. The spectrum has been built for events satisfying the MB photon trigger.*

For each reaction class, the corresponding hard photon spectrum is fitted to the double exponential distribution, Eq. (6.2), to extract the direct hard photon yield. From the number of measured direct hard photons, $N_\gamma^d(RC)$, and of the charged particles detected in each reaction class, $N_R(RC)$, the direct hard photon multiplicity is computed according to:

$$M_\gamma^d(RC) = \frac{1}{\varepsilon_\gamma} \cdot \left(\frac{SD}{T}\right)_{\gamma * DB} \cdot \left(\frac{T}{SD}\right)_R \cdot \frac{N_\gamma^d(RC)}{N_R(RC)} \tag{7.9}$$

where ε_γ is the photon efficiency and the factors $(SD/T)_{\gamma * DB}$ and $(SD/T)_R$ are the ratio of the scale-down factor to the life time of the minimum bias photon trigger and of the MB particle trigger, respectively. The only difference between the former expression and the inclusive M_γ^d from Eq. (6.13) concerns the considered efficiencies. Since the exclusive

Reaction class	Multiplicity condition	$\%\sigma_R$	$\%\sigma_R(\gamma$*DB)
A or Peripheral	M^{DB+FW} = 1-2 and (M^{SSD} (at $\theta < 5$) = 0)	57%	23%
B	M^{DB+FW} = 1-2	67%	26%
C	$2 < M^{DB+FW} < 8$	38%	58%
D	$5 < M^{DB+FW} < 9$	10%	24%
E	$6 < M^{DB+FW} < 10$	7%	18%
F or Central	$9 < M^{DB+FW} < 15$	2%	6%

Table 7.1: *Condition on the fragment multiplicity in the SSD (M^{SSD}), the charged particle multiplicity (IMF + LCP) in the DB (M^{DB}) and the FW (M^{FW}) that define each reaction class. The contribution to the reaction cross-section and to the nuclear reactions detected by the photon photon MB trigger for each reaction class are also reported.*

photon measurements are performed after selecting a particular range in the total charged particle distribution, the DB efficiency factor (ε_R) is canceled in Eq. (7.9), and hence only the TAPS efficiency (ε_γ) is present in the exclusive hard photon multiplicity expression.

The experimental M_γ^d, $\langle N_{pn}\rangle$ and $\langle$b$\rangle$ values that characterize the selected reaction classes are listed in Table 7.2 (see also Fig. 7.3). The errors associated to each $\langle$b$\rangle$ are obtained by employing expression (7.6) for $N_{pn}(\mathrm{RC})^{\pm} = N_{pn}(\mathrm{RC}) \pm \Delta\mathrm{N}$. The asymmetric error of the M_γ^d measured for reaction class F comes from the use of an average upper limit in the double source fit of the hard photon spectrum.

Reaction class	M_γ^d	$\langle N_{pn}\rangle$	$\langle$b$\rangle$ (fm)
A or Peripheral	$(3.24 \pm 0.19)\cdot10^{-4}$	4.14 ± 0.55	9.2 ± 0.3
B	$(4.07 \pm 0.26)\cdot10^{-4}$	5.19 ± 0.62	8.8 ± 0.3
C	$(1.46 \pm 0.08)\cdot10^{-3}$	18.64 ± 2.17	5.9 ± 0.5
D	$(2.40 \pm 0.15)\cdot10^{-3}$	30.65 ± 3.73	4.0 ± 0.6
E	$(2.83 \pm 0.15)\cdot10^{-3}$	36.14 ± 4.44	3.1 ± 0.7
F or Central	$(3.83\ ^{+0.40}_{-0.35})\cdot10^{-3}$	48.91 ± 6.69	1.3 ± 1.1

Table 7.2: *Measured direct photon multiplicity (M_γ^d), average number of first chance proton-neutron collisions $\langle N_{pn}\rangle$, and associated averaged impact parameter $\langle b\rangle$ obtained from the model [36] for each one of the six studied reaction classes.*

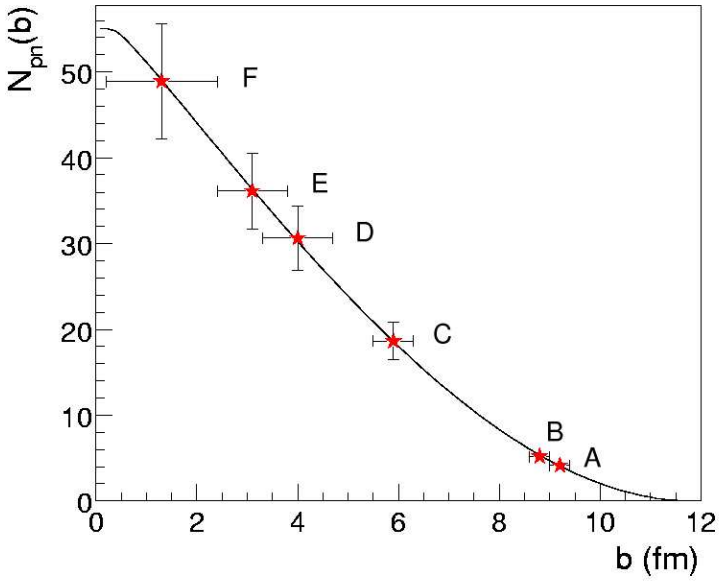

Figure 7.3: *Number of proton-neutron collisions N_{pn} as a function of the impact parameter b, computed from Eq. (7.6). The stars represent the experimental $\langle N_{pn} \rangle$ of each reaction class obtained from the measured direct hard photon multiplicity.*

7.3.1 Impact parameter cross-checking

In Section 6.4.2 we show that the experimental (efficiency corrected) reaction cross-section σ_R^{exp} is in good agreement with the geometrical one, as assumed by the geometrical procedure for the estimation of the impact parameter (Section 7.2.1). We have applied this method in order to test the validity of the impact parameters measured from M_γ^d, since both independent techniques should provide compatible results.

We have considered that the DB was not efficient for the most peripheral events, as indicated by FREESCO simulations [26]. Therefore, the experimental b_{max} has been deduced from Eq. (7.1) using the σ_R^{exp} measured without applying the efficiency correction factor, $\varepsilon_R = 0.76$ (6.4.2). Employing Equation 7.4 we have calculated the relation between the (inclusive) total charged particle multiplicity M_{cp}^{TOT} and the impact parameter. The result is shown in Figure 7.4.

For a given reaction class, the associated impact parameter $\langle \mathrm{b} \rangle_{geo}$ has been estimated as the average of the $\mathrm{b}(M_{cp}^{TOT})$ values, which have been weighted by the relative contri-

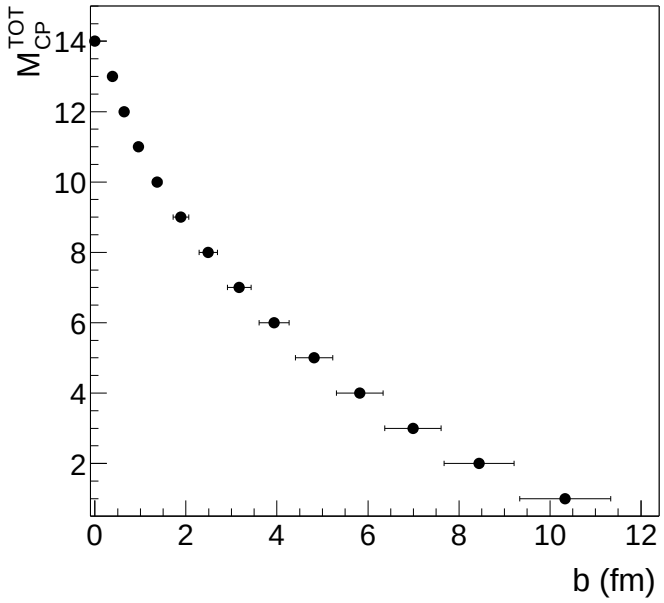

Figure 7.4: *Total charged particle multiplicity as a function of the geometrical impact parameter. This relation is obtained by means of the geometrical method ([94], see 7.2.1).*

Reaction class	$\langle M_{cp}^{TOT} \rangle$	$\langle b \rangle_{geo}$ (fm)
A or Peripheral	1.5	$9.4 \pm 0.8^{\star}$
B	1.5	9.4 ± 0.8
C	4.7	5.2 ± 0.4
D	6.8	3.3 ± 0.3
E	7.8	2.6 ± 0.2
F or Central	11.4	0.9 ± 0.1

Table 7.3: *Average charged particle multiplicity M_{cp}^{TOT} and impact parameter $\langle b \rangle$ of each reaction class estimated using the total charged multiplicity ($\star$ see text).*

bution of each M_{cp}^{TOT} to the reaction class. The weighting factors have been determined from the M_{cp}^{TOT} distribution measured by means of the MB photon trigger. The obtained $\langle b \rangle_{geo}$ (Table 7.3) are in good agreement with the ones calculated by means of the direct hard photon multiplicity (Table 7.2), thus confirming the former impact parameter measurements. Despite this agreement, the monotonous variation of M_{cp} with b assumed by the geometrical method is not valid for central collisions, since the maximum M_{cp}^{TOT} does

not correspond to a real b=0. So, for this cross-checking we only consider peripheral and semicentral reactions. Concerning reaction class A, since for this reaction class the condition on the total charged particle multiplicity is the same as for reaction B (M^{DB+FW} = 1-2), the average impact parameter cannot be distinguished from the one of reaction B, using this method.

7.4 Determination of the impact parameter for reactions where a hard photon is produced

We attempt to exploit the radiation of the thermal hard photon component as a tool to extract the thermodynamical state of the source and its dependence on the centrality, equivalently on the $\epsilon^{\star}$, of the collision. So, it is of crucial importance to assess the impact parameter for the particular reactions where a hard photon is produced as precisely as possible. With regard to this requirement, for a given reaction class (RC), defined by a window in the M_{cp}^{TOT} distribution, the hard photon production may be biased through the higher M_{cp}^{TOT} values (see discussion in the former Section). Hence, the $\langle$b$\rangle$ calculated by means of the previous method(s) may be overestimated for reactions where a hard photon is produced. Whereas the difference between the estimated $\langle$b$\rangle$ and the impact parameter when a hard photon is detected might be minor for RC accounting for a low $\% \sigma_R$, in our case defined by a narrow M_{cp}^{TOT} gate, the b distribution might exhibit a non negligible shift for RC covering a wide σ_R region. That may be the case of the b estimated for reaction class C and definitely for the average inclusive impact parameter. How can the b of particular reactions, where a hard photon is produced, then quantitatively be estimated?

For those reactions were a hard photon is produced, the σ_R(b) is modulated by the number of pn collisions N_{pn}, whose dependence on b is given by the equal-participant geometrical model (Eq. (7.4)). As a consequence the ratio between the σ_R(b) and the total (integrated over b) σ_R is a representable function sensitive to the deviation through lower b (see Figure 7.5).

Applying the geometrical model to the total charged particle distribution for reactions where a hard photon is emitted, for a given value of M_{cp}^{TOT} the associated $\sigma_R(M_{cp}^{TOT})/\sigma_R$ corresponds to the same value of σ_R(b)$/\sigma_R$. Thus, it is possible to estimate the average impact parameter for reactions where a hard photon is emitted by correlating the experimental $\sigma_R(M_{cp}^{TOT})/\sigma_R$ and the theoretical σ_R(b)$/\sigma_R$. The average b of each reaction class

has been obtained with this method after weighting the $b(M_{cp}^{TOT})$ by the contribution of each M_{cp}^{TOT} to the RC. Table 7.4 reports the $\langle b \rangle$ estimated for each RC for reactions where a hard γ is emitted.

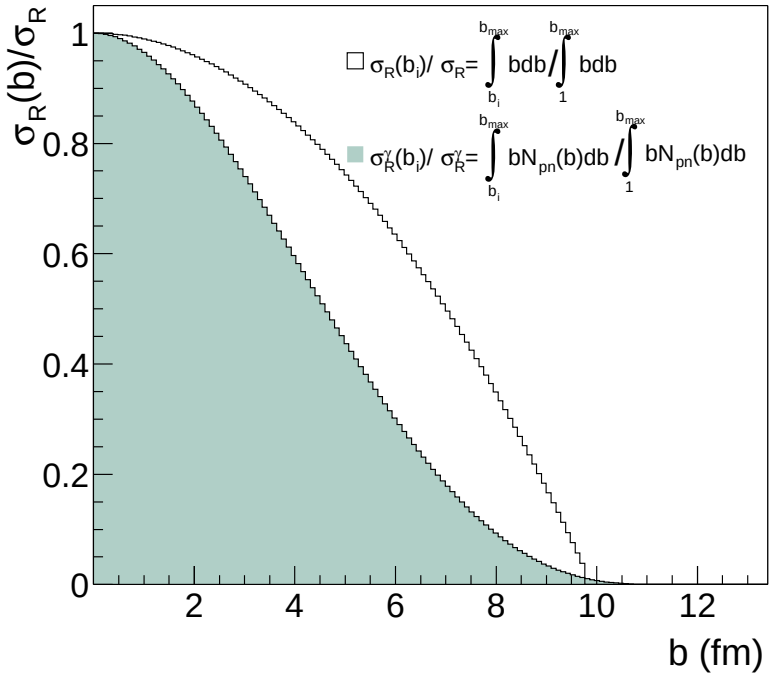

Figure 7.5: *Evolution of $\sigma_R(b)/\sigma_R$ as a function of the impact parameter without and with (dark spectrum) the condition of measuring a hard photon.*

Reaction class	$\langle b \rangle_{geo}$ (fm)
Class A or Peripheral	7.6 ± 0.3
Class B	7.2 ± 0.3
Class C	4.2 ± 0.4
Class D	2.8 ± 0.4
Class E	2.2 ± 0.6
Class F or Central	1.0 ± 0.9

Table 7.4: *Average impact parameter $\langle b \rangle$ estimated for reactions where a hard photon is produced.*

7.5 Centrality dependence of the hard photon production

The two-exponential fit of Equation (6.2) reproduces the hard photon energy spectrum of each one of the six reaction classes, from peripheral to central events. The values of the direct and thermal inverse slope parameters and relative intensities obtained from the best least-square fit are listed in Table 7.5.

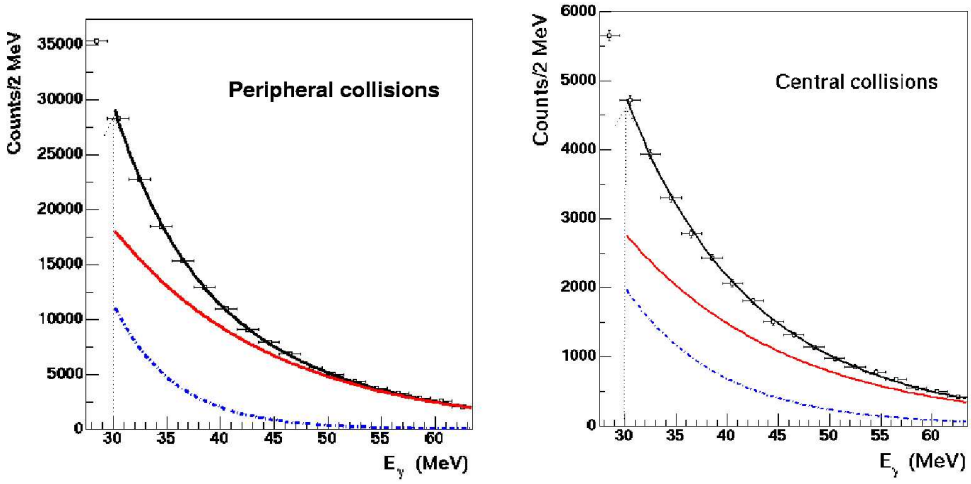

Figure 7.6: *Hard photon energy spectra measured in the region $E_\gamma = 30$ - 65 MeV for the most peripheral and central reaction classes. The thermal (dashed line) and direct (solid line) exponential distributions are shown. The spectra have been plotted in a linear scale to emphasize the thermal contribution in both cases.*

Reaction class	E_0^d (MeV)	E_0^t (MeV)	I_t/I_{tot}(%)	M_γ^t	χ^2/ndf
A	14.9 ± 0.9	5.7 ± 0.5	19 ± 1	$(7.60 \pm 0.72)\cdot10^{-5}$	1.5
B	14.6 ± 0.9	5.7 ± 0.5	19 ± 1	$(8.93 \pm 1.08)\cdot10^{-5}$	1.2
C	15.6 ± 0.9	6.3 ± 0.6	19 ± 1	$(3.40 \pm 0.43)\cdot10^{-4}$	1.0
D	16.0 ± 1.0	7.8 ± 0.7	25 ± 1	$(7.80 \pm 0.57)\cdot10^{-4}$	1.4
E	16.1 ± 1.1	7.9 ± 0.7	25 ± 1	$(9.43 \pm 0.61)\cdot10^{-4}$	1.2
F	15.9 ± 1.0	8.7 ± 0.8	27 ± 2	$(1.42\ ^{+0.22}_{-0.32})\cdot10^{-3}$	1.0

Table 7.5: *Characteristics of the hard photon spectra measured in the 6 different centrality classes: direct (E_0^d) and thermal (E_0^t) slopes, the ratio of thermal to total hard-photon intensities (I_t/I_{tot}) and the thermal photon multiplicity (M_γ^t).*

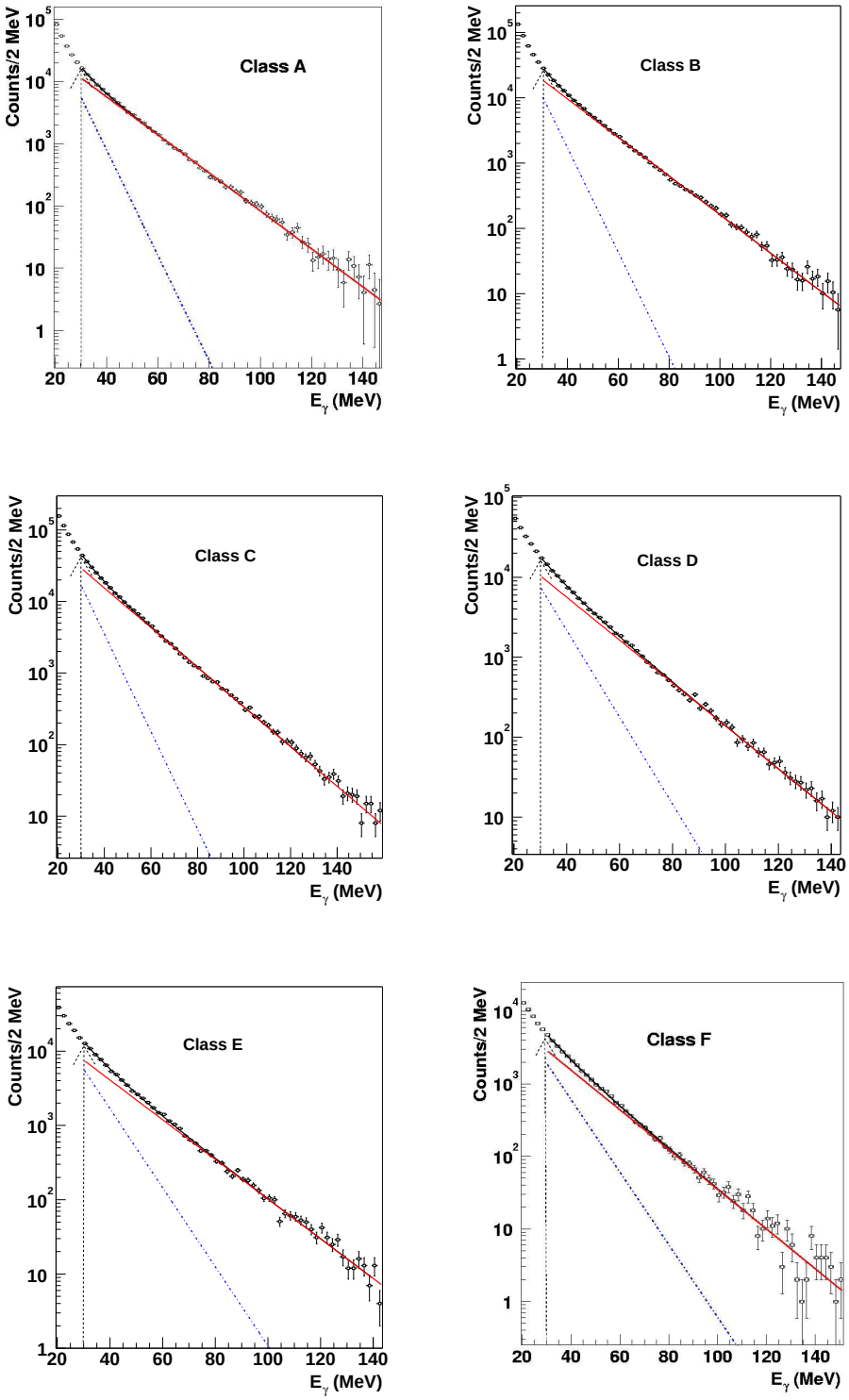

Figure 7.7: *The hard photon energy spectra measured in each reaction class, from the most peripheral case (reaction class A) to the most central class (reaction class F). The spectra have been fitted according to Eq. (6.2) in the energy range E_γ = 30 - 130/160 MeV. The thermal (dashed line) and direct (solid line) exponential distributions are shown.*

The contribution of the thermal hard photon emission to the total hard photon spectrum is not negligible ($I_t/I_{tot} \geq 19\%$) in any of the selected reactions. The evolution of the direct and thermal hard slopes and yields with the centrality are discussed in the next two sections.

7.5.1 Direct and thermal hard photon slopes

For each one of the 6 reaction classes the direct and thermal slopes normalized to the inclusive direct and thermal slope values are displayed as a function of the reduced impact parameter b/b_{max} in Figs. 7.8 and 7.9, respectively. Such a representation allows to compare the relative variation of both slopes with the reaction centrality. Whereas the measured E_0^t(b) differ up to 24% from the inclusive value, the direct slope does not vary within the errors from the inclusive E_0^d. A small decrease of the hard photon hardness

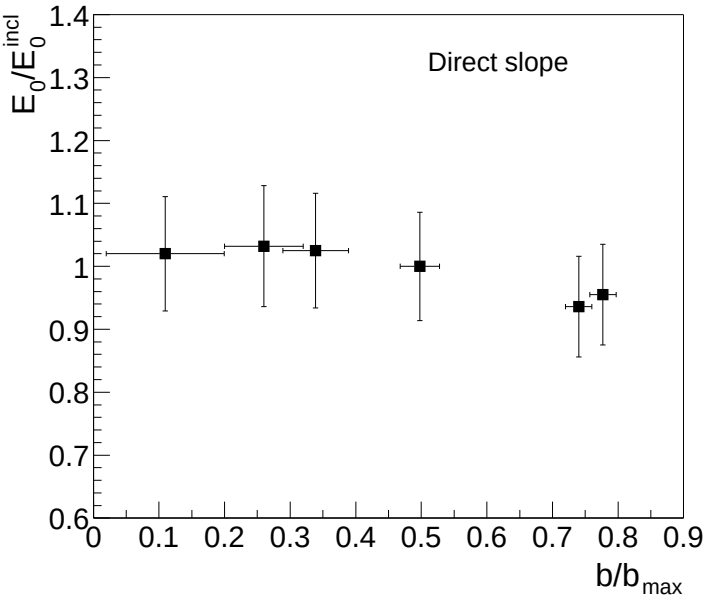

Figure 7.8: *Variation of the direct hard photon slope measured in 6 different centralities in ^{129}Xe + ^{nat}Sn reactions at 50A MeV, normalized to the inclusive value, as a function of the reduced impact parameter.*

from central to peripheral collisions has been observed [95, 33, 96, 102, 25] and understood by preequilibrium phase-space population arguments [102]. The E_0^d variation with centrality measured in the present experiment is lower than expected on basis of previous

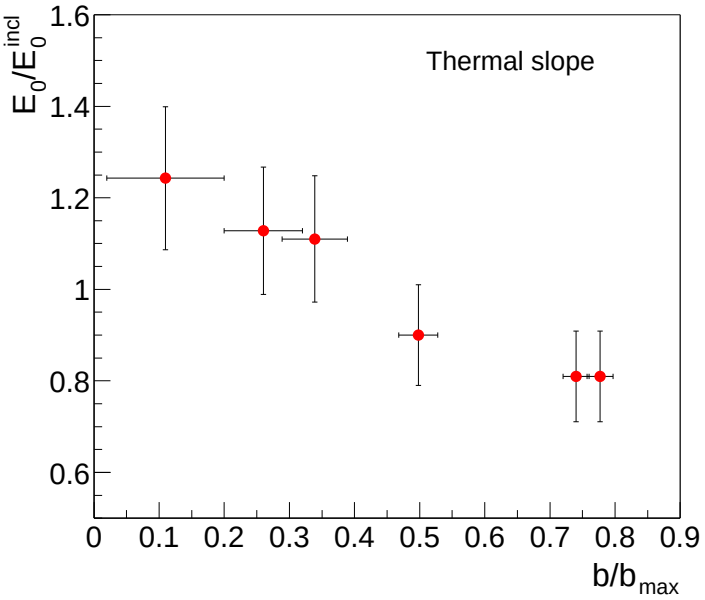

Figure 7.9: *Variation of thermal slope measured in 6 different centralities in ^{129}Xe + ^{nat}Sn reactions at 50A MeV, normalized to the inclusive value, as a function of the reduced impact parameter.*

measurements, whereas the dependence of the thermal slope on the impact parameter is more compatible with the observed hard photon behavior in former single source analyses. That could be an indication of the important weight the thermal component should have in (some) previous exclusive hard photon measurements. The thermal slope evolution with the centrality reflects the larger excitation energies, and hence temperatures, reached in small impact parameter reactions. The measurement of an almost constant direct slope confirms that the E_0^d might be considered as an observable mainly dependent on the bombarding energy. However, we have to keep in mind that we are not sensitive to the most peripheral reactions, for which a change in the direct hard photon slope cannot be discarded from the present analysis.

7.5.2 Direct and thermal hard photon yields

In Figure 7.10 the direct and thermal hard photon multiplicities, normalized to the inclusive direct and thermal multiplicity values, have been plotted as a function of the reduced impact parameter. The multiplicity of both components follow a very similar evolution

with the impact parameter, as already suggested by the $M_\gamma(M_{CP}^{DB})$ measurements described in Section 7.1.

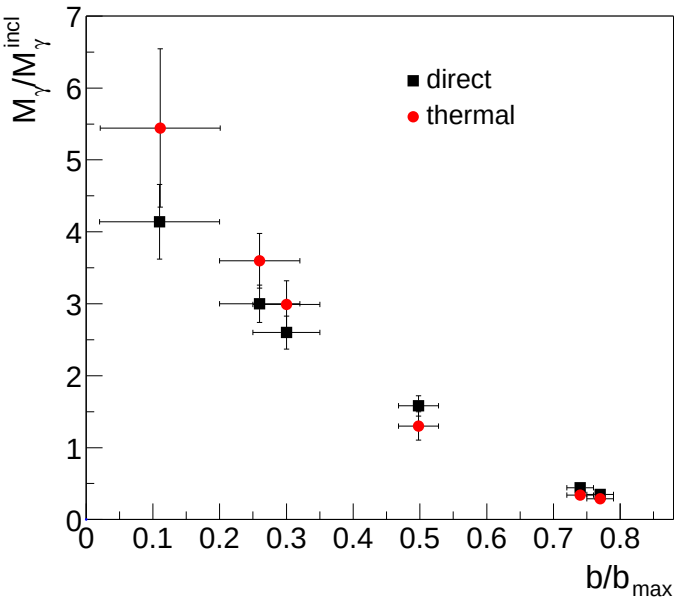

Figure 7.10: *Variation of the direct and thermal hard photon yields measured in 6 different centralities in ^{129}Xe + ^{nat}Sn reactions at 50A MeV, normalized to the inclusive values, with the reduced impact parameter.*

One could think that the similar behavior of direct and thermal bremsstrahlung components with the centrality could be connected to a contemporary pnγ emission.

That can be solved in Figure 7.11, where the values of the thermal (direct) slopes are displayed as a function of the thermal (direct) multiplicities. The evolution of the direct hard photon slope is independent of the direct hard photon multiplicity. This behavior shows that the increase of the direct hard γ multiplicity with the centrality is just a consequence of the augmentation of the number of first-chance pnγ collisions. At variance with the direct multiplicity, the thermal M_γ exhibits a linear dependence on the slope . On the other hand, the size of the thermalized source ($\approx A_1 + A_2$) remains almost constant with centrality. Therefore, the linear relation M_γ^t and E_0^t indicates that the evolution of the thermal hard photon yield with the centrality is only due to the increase of the excitation energy and, thus, of the energy available in secondary collisions.

Therefore, the conditions responsible of the evolution of both multiplicities with the centrality must be different. One way to compare the exclusive thermal and direct yields

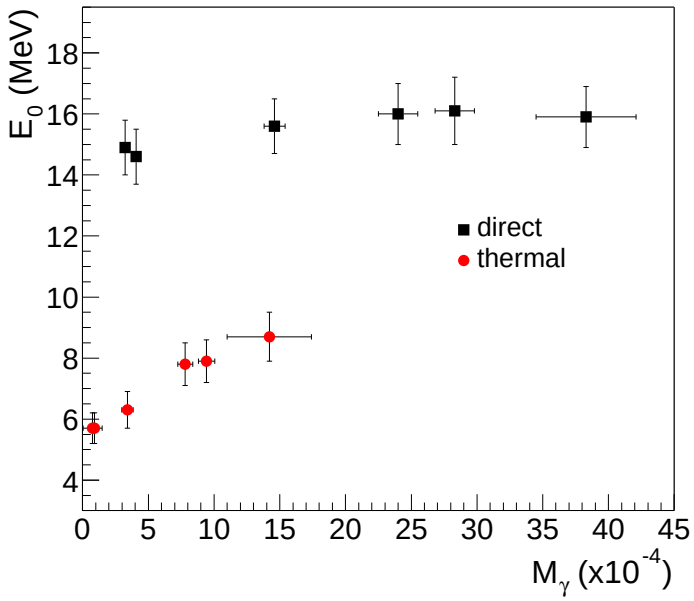

Figure 7.11: *Variation of the direct and thermal hard photon slopes measured in 6 different centralities in ^{129}Xe + ^{nat}Sn reactions at 50A MeV as a function of the direct and thermal multiplicity, respectively.*

for the Xe+Sn system with the thermal and direct inclusive M_γ measured for different reactions is to display the multiplicities as a function of the average number of first chance pn collisions. For each reaction class $\langle N_{pn}(RC)\rangle$ is represented in the left panel of Fig. 7.12. Both M_γ follow a clear linear dependence on N_{pn}.

The slope of the direct multiplicity[2] is equal to the direct hard photon probability $P^d_\gamma(K_{lab})$, as expected for incoherent first chance pnγ emission. The linear dependence of the energy available in secondary pnγ collisions on the centrality shows up in the correlation between the thermal M_γ and the number of (first chance) N_{pn}. There is a threshold in the number of (first chance) pn collisions necessary to measure a thermal emission. This result is consistent with the existence of a minimum volume above which the chance of stopping and thermalization is high enough to observe a thermal emission

[2]The total M_γ is represented instead of the direct M_γ in the left panel of Fig. 7.12 in order to compare our results with the ones reported in [26](right panel of the same figure).

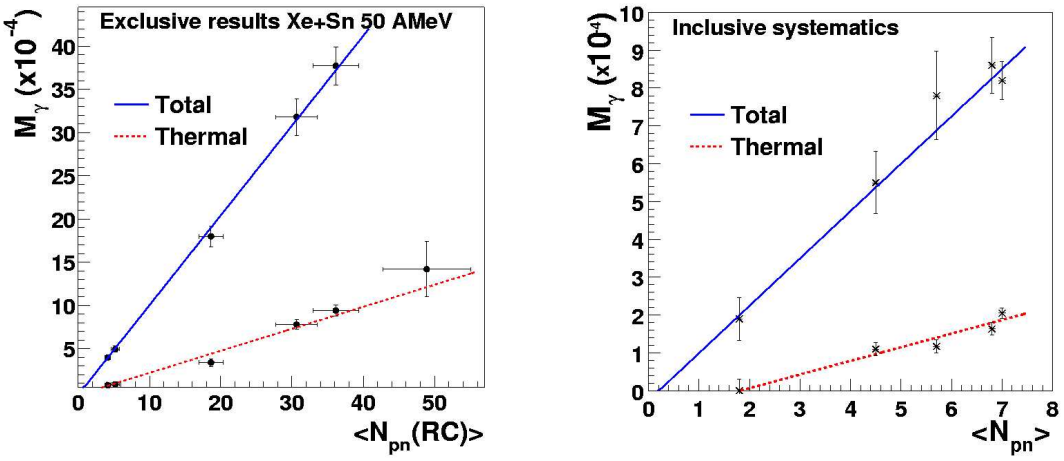

Figure 7.12: *Total (direct + thermal) and thermal hard photon multiplicities as a function of the number of first-chance pn collisions. Left panel: the measurements correspond to the six ^{129}Xe + ^{nat}Sn at 50A MeV reaction classes reported in this work. Right panel: inclusive systematics collected from 4 different systems at 60AMeV [40, 26].*

[26]. The most interesting point of these exclusive $M_\gamma(\langle N_{pn}(RC)\rangle)$ measurements is that they exhibit the same behavior as the one of the inclusive measurements collected from 4 different HI reactions at 60AMeV [26] (right panel of Fig. 7.12). Such a result proves the consistency of our measurements.

7.6 Multifragmentation reactions

Besides investigating the hard photon production dependence on the impact parameter, the hard photon spectrum measured in multifragmentation ^{129}Xe + ^{nat}Sn reactions at 50A MeV has been analyzed. We have defined as multifragmentation reactions those where at least three intermediate-mass-fragments are detected in the Dwarf Ball, $M^{DB}_{IMF} > 3$. By excluding the IMF measured in the Forward Wall we avoid the contamination of peripheral reactions, where fragments coming from the (quasi-projectile) are forward emitted. Unfortunately, the identification of IMF by the DB in the present setup was only possible up to Z=10. The restricted identification was even worsened by the low detection efficiency of the inner DB phoswiches. These experimental conditions, together with the small cross section of multifragmentation reactions, lead to an amount of detected multifragmentation reactions which only corresponds to 2% of the total reaction cross

section.

Still, the hard photon spectrum can be properly reproduced by a double source distribution (see Figure 7.13), the parameters obtained in such a fit are reported in Table 7.6. The measured direct and thermal inverse slopes and relative intensities are compatible with the ones measured for the inclusive spectra. The thermal slope and relative intensity for multifragmentation are lower than those measured for the most central reaction class (Table 7.5). Concerning this result, the direct hard γ multiplicity for multifragmentation reactions is closer to the one measured for reaction class C $(1.46 \pm 0.08)\cdot 10^{-3}$ than to the M_γ^d for central reactions. This is an evidence that due to the low probability of detecting

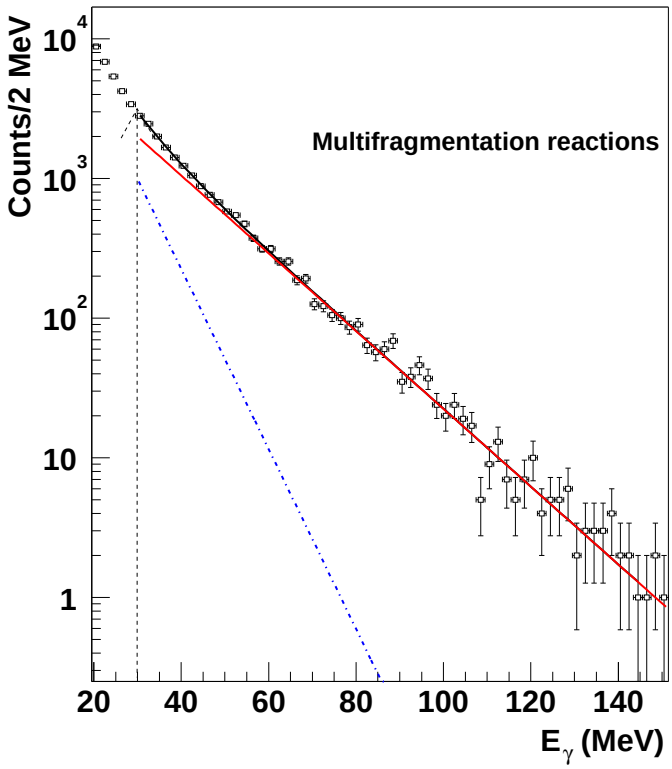

Figure 7.13: *Hard photon energy spectrum measured for reactions where $M_{IMF}^{DB} > 3$. The spectrum has been fitted according to Eq. (6.2). The thermal (dashed line) and direct (solid line) exponential contributions are shown.*

reactions where $M_{IMF}^{DB} > 3$, the measured multifragmentation events form a subgroup of (semicentral) reaction class C, which exhibits the largest hard photon statistics of all selected reaction classes. Still, the measurement of a thermal hard photon emission in

E_0^d (MeV)	E_0^t (MeV)	I_t/I_{tot}(%)	M_γ^d	M_γ^t	χ^2/ndf
15.7 ± 1.1	7.6 ± 1.0	20 ± 3	$(1.70 \pm 0.14)\cdot10^{-3}$	$(4.24 \pm 0.71)\cdot10^{-4}$	1.1

Table 7.6: *Direct and thermal slopes, ratio of thermal to total intensities and direct and thermal multiplicities deduced from the hard photon spectrum measured for multifragmentation reactions.*

the identified multifragmentation reactions indicates that the source has reached thermal equilibrium before fragmenting. This result agrees with those obtained from the distribution of excitation energies of the primary fragments measured by the INDRA collaboration in dedicated investigations on the ^{129}Xe + ^{nat}Sn at 50A MeV multifragmentation [45].

7.7 Exclusive analysis of the GDR emission

Exploiting the wide dynamic range of TAPS, we have estimated the γ yield from the GDR decay emitted in peripheral ^{129}Xe + ^{nat}Sn reactions. The main motivation of this investigation was to identify a possible thermal and GDR mixture in the low energy range of the hard photon spectra. Such a contamination could distort the measurement of the thermal hard photon slope and yield, mostly in the peripheral reaction classes for which the observed thermal emission is softer. Moreover, the reached excitation energies at these large impact parameter reactions can still be not high enough for suppression of the collective mechanisms responsible for the GDRγ emission.

In order to perform the GDRγ analysis the direct and thermal hard photon components have been subtracted from the total photon spectra. This subtraction is done by extrapolating the double hard γ exponential fit down to the lowest photon energy, the TAPS LED threshold of 10 MeV. This extrapolation technique is routinely applied in GDR measurements from HI reactions (see e.g. [103, 104, 92]). Even if a single hard photon exponential is considered in those works that continues being consistent for low hard photon statistics.

7.7.1 GDR yield in peripheral reactions

We have compared the GDR spectra measured for peripheral reaction classes A and B with the GDR distributions measured with the BaF_2 multidetector MEDEA and reported by T.

Suomijärvi *et al.* [92]. In this work the GDRγ emission from hot nuclei of A $\approx$ 115 formed in the ^{36}Ar + ^{90}Zr at 27A MeV reaction is investigated in detail. The comparison of the GDRγ yield measured in this analysis with the one measured for peripheral reactions in our work comes easily to mind when considering the similarities in mass and in excitation energy of the emitting sources:

- In peripheral ^{129}Xe + ^{nat}Sn reactions the quasi-projectile and quasi-target are close to the ^{129}Xe and ^{nat}Sn masses, then scaling the photon spectrum measured in these reaction classes by a factor $\sim$ 1/2, the GDR yield can be compared with the one emitted by single nuclei of A $\approx$ 115;
- Despite the different geometry and bombarding energy of both reactions, the excitation energies reached at large impact parameters in ^{129}Xe + ^{nat}Sn reactions ($\sim$ 3A MeV, see section 8.3) are comparable with the $\epsilon^{\star}$ populated in the ^{36}Ar + ^{90}Zr MeV reaction at 27A. Besides, the GDR yield measured for the ^{36}Ar + ^{90}Zr system has been found to remain constant with the excitation energy (see Fig.7.14).

The GDR yields (the γ spectra after subtraction of the bremsstrahlung contribution) for the ^{36}Ar + ^{90}Zr reaction for $\epsilon^{\star} = 350$ MeV and for $\epsilon^{\star} = 500$ MeV[92], and the GDR yield estimated for the ^{129}Xe + ^{nat}Sn reaction class A are plotted together in Figure 7.14. The GDR yield measured for reaction class B is almost identical to the one measured for class A, so the first one has not been added to the figure. The GDR distributions measured with MEDEA are in a very good agreement with the GDR yield estimated for peripheral ^{129}Xe + ^{nat}Sn reactions. The small difference between both reaction spectra at the low dM/dE bins might be connected to the slightly lower excitation energy estimated for peripheral ^{129}Xe + ^{nat}Sn reactions. Besides, it has to be taken into account that the bremsstrahlung component, subtracted from the spectra, is represented by a single exponential function for the MEDEA reaction, whereas the double exponential distribution is considered for reaction class A (and B).

The global compatibility of the three distributions assures the validity of the estimation of the GDR yield for the peripheral Xe+Sn hard photon spectra. Taking into account that for peripheral reactions the total photon multiplicity around 30 MeV is $M_{\gamma} \approx 9 \cdot 10^{-5}$ and that the GDR yield at this energy for all systems considered here is found to be lower than 10^{-5} (see Fig.7.14), we can conclude that the GDR contamination at the low energy range of the peripheral hard photon spectra can be neglected and then, that the measured thermal hard photon parameters are basically undistorted.

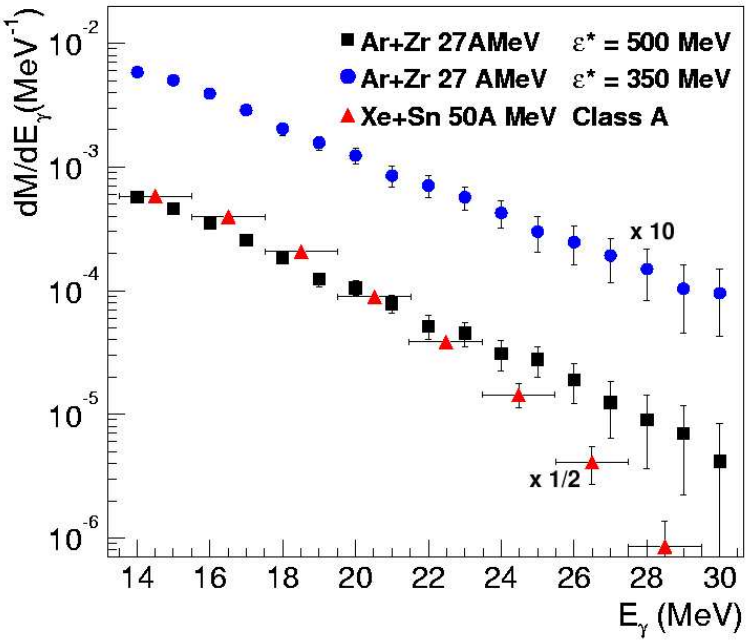

Figure 7.14: *Experimental γ spectra after subtraction of the bremsstrahlung contribution for the $^{36}Ar + ^{90}Zr$ reaction: $\epsilon^* = 350$ MeV, (dots) $\epsilon^* = 500$ MeV (squares)[92], and for the $^{129}Xe + ^{nat}Sn$ reaction class A (triangles).*

7.7.2 GDR slope behavior with centrality

After investigating the direct and thermal hard photon slope dependence on the centrality (7.5.1), we have performed the same investigation for the GDRγ component. Unlike the thermal hard photon slopes, the measured values of GDR slopes remain constant as a function of centrality (see Fig.7.15). This result is in good agreement with the slope saturation observed by the MEDEA collaboration [92].

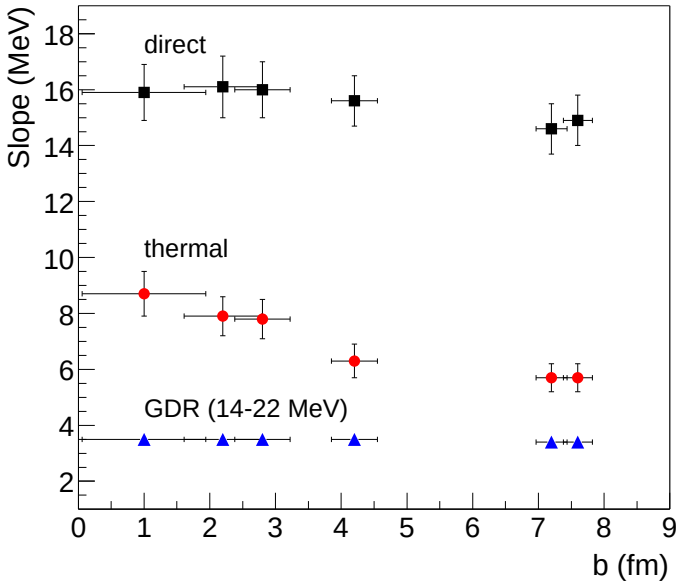

Figure 7.15: *Exclusive slope parameters of the direct (squares) and thermal (circles) bremsstrahlung components, and of the spectra after subtraction of both bremsstrahlung components between 14 and 22 MeV (triangles).*

7.8 Summary of results

The conjunction of high statistics data and a complete experimental setup with photon and charged particle detection capabilities has allowed to systematically investigate for the first time the dependence of the thermal hard photon production on centrality. For the ^{129}Xe + ^{nat}Sn reaction at 50A MeV we have carried out a double source analysis for 6 different impact-parameter classes ($0.1 \leq b/b_{max} \leq 0.6$) and for multifragmentation reactions.

- We have employed a new technique to estimate the impact parameter for reactions in which a hard photon is detected. This method takes into account the impact parameter biases through semicentral collisions occurred in reactions where a hard photon is produced.

- We have measured a thermal hard photon emission along all the covered impact parameter range. The thermal contribution to the total hard photon production

amounts from 19% for peripheral collisions, up to 27% for central ones.

- The direct hard photon slope remains practically constant, $E_0^d \approx 15.5$ MeV, as a function of impact parameter. The measured thermal hard photon slope increases with the number of first-chance *pn* collisions, i.e. with centrality. This behavior is consistent with the linear dependence of the E_0^t on the available energy in the nucleus-nucleus center of mass observed for the inclusive systematics [42].

- Both thermal and direct yields show a linearly increasing dependence on the centrality. However, at variance with the direct multiplicity, the M_γ^t follows a linear dependence on the thermal slope, reflecting hence the correlation between the thermal emission and the temperature. The lower $M_\gamma^t(N_{pn})$ slope reflects the less energy available in secondary nucleon-nucleon collisions. This result is in very good agreement with the one obtained in inclusive hard photon results for different reactions. Moreover, higher (thermal) multiplicities are reached in the exclusive hard photon analysis, independently of the system, by selecting the most central collisions.

- The hard photon spectrum for the detected multifragmentation reactions also features a thermal component, whose characteristics are compatible with the ones measured in the inclusive spectra. Nevertheless, due to limitations of our setup, the identified multifragmetation reactions correspond only to a small fraction of *semicentral* reactions.

- The estimation of the GDR gamma yield $M_\gamma \leq 10^{-5}$ in peripheral ^{129}Xe + ^{nat}Sn reactions has allowed to discard any possible contribution of the GDR decay component in the low energy part of the peripheral hard photon spectra.

These results indicate that the excited nuclear systems produced in ^{129}Xe + ^{nat}Sn reactions at 50A MeV attain a thermally equilibrated state, from which the second hard photon component is emitted, in all the range of considered impact parameters. The undistorted image that (thermal) photons provide is a valuable tool to derive the thermodynamical properties of the equilibrated system as a function of excitation energy. This investigation will be presented in the next chapter.

Chapter 8

Complements to the caloric curve

In this chapter we exploit the features of the emission of thermal hard photons to derive the thermodynamical properties of excited nuclear systems at equilibrium. We have extracted the temperature of the thermalized composite systems formed in the Xe + Sn reactions for the different centralities investigated in the preceding chapter. In the second section, we take benefit of thermal hard photon emission to estimate the lifetime of the thermalized source formed in the different pertinent reactions. Finally in the last section, after estimating the excitation energy $\epsilon^\star$ for each Xe + Sn reaction class, we have constructed the caloric curve, which relates $\epsilon^\star$ and T.

8.1 Measurement of the nuclear temperature

The slope of the thermal hard photon spectrum E_0^t is strongly correlated with the temperature T of the emitting source (however, since the photon-hadron coupling is very weak, thermal hard photons are not in thermal equilibrium with the source, i.e. they do not exhibit a black body spectrum). A thermal model is needed to quantitatively deduce the relation between E_0^t and T. We have used here the kinetic thermal model of Neuhauser and Koonin [105]. The electromagnetic radiation rate (number of photons per fm^3 and per fm/c) emitted by a hot and equilibrated nuclear fragment is calculated by this model as a function of the local density and temperature of the source. They assume that incoherent proton-neutron bremsstrahlung collisions are the main source of photon emission for $E_\gamma > 30$ MeV (see Appendix A for a detailed description of the Koonin and Neuhauser thermal model).

The hard photon spectra thus calculated can be well approximated by an exponential

with slope E_0^t. The evolution of E_0^t values extracted from a fit above 30 MeV with the temperature is quantitatively well described by the following linear expression:

$$T(\text{MeV}) \; = \; (0.78 \; \pm \; 0.02) \cdot E_0^t(\text{MeV}) \tag{8.1}$$

in the region T $\approx$ 3 - 10 MeV and density $\rho \approx (0.3 - 1.2)\rho_0$, and for nuclear densities close to the saturation value $\rho_0 = 0.17 \; fm^{-3}$.

The thermal hard photon slope can be therefore considered as a nuclear thermometer of the excited radiating nuclear matter. This novel nuclear thermometer presents important advantages with respect to the conventional (charged particle) methods [8] based on the relation of the temperature to various particle observables: the double isotopic yield ratio (isotopic temperature), the kinetic energy spectra of light charged particles (kinetic temperature), and the excited state populations. The characteristics of the photon thermometer are the following:

- Absence of final state distortions. Due to the weak photon electromagnetic coupling of photons with nucleons, the slope parameter of the hard photon spectrum is not modified after emission.

- Measurement of the initial temperature of the nuclear system. Thermal hard photons are emitted just after equilibration of the source, when the maximum temperature is reached [42].

We have applied this photon thermometer to extract the temperature of the source issued from the different centrality ^{129}Xe + ^{nat}Sn reactions studied in this work. The obtained temperatures are reported in Table 8.1 and are represented as a function of the centrality in Fig. 8.1. The temperature of the nuclear system exhibits a slight increasing behavior (4.4 $\rightarrow$ 6.8 MeV) from the peripheral reaction class A ($b/b_{max} \approx 0.6$) to the central reaction class F ($b/b_{max} \leq 0.1$). This result is in very good agreement with the one observed from the inclusive thermal hard photon slope systematics. For the 7 reactions where a thermal hard photon component has been measured with TAPS, including the present Xe+Sn system, the highest T values are observed in the systems with higher available energy in the nucleus-nucleus center-of-mass [106] (see Table A.1 in Appendix A). Interestingly, in ^{129}Xe + ^{nat}Sn the range of temperatures obtained from the different centralities is practically the same as the one sampled by the former different systems studied by the TAPS Collaboration ($T \approx$ 4.3-6.9 MeV).

Reaction class	E_0^t (MeV)	T (MeV)
Inclusive	7.0 ± 0.6	5.5 ± 0.8
A or Peripheral	5.7 ± 0.5	4.4 ± 0.4
B	5.7 ± 0.5	4.4 ± 0.4
C	6.3 ± 0.6	4.9 ± 0.5
D	7.8 ± 0.7	6.1 ± 0.5
E	7.9 ± 0.7	6.2 ± 0.5
F or Central	8.7 ± 0.8	6.8 ± 0.6

Table 8.1: *Nuclear temperatures T estimated through Eq. (8.1) from the experimental thermal hard photon slopes E_0^t of the inclusive and exclusive hard photon spectra measured for $^{129}Xe + ^{nat}Sn$ at 50A MeV.*

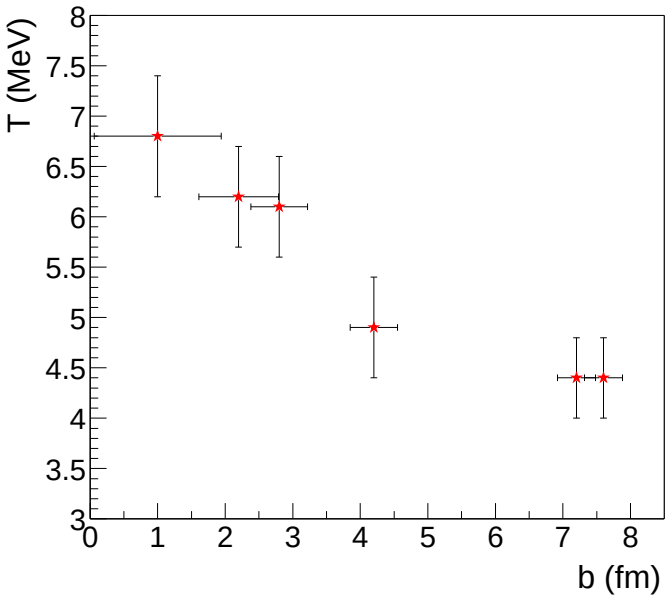

Figure 8.1: *Nuclear temperature as a function of the impact parameter estimated for $^{129}Xe + ^{nat}Sn$ at 50A MeV.*

8.2 Lifetime of the thermalized system

The multiplicity of hard photons emitted by an equilibrated nuclear fragment of density ρ and temperature T can be calculated by means of the model of Neuhauser and Koonin from the following expression:

$$M_\gamma^{NK} = \int d^3x \int dt \int_{30}^{\infty} \frac{dR_\gamma^{NK}(T,\rho)}{dE_\gamma} dE_\gamma \tag{8.2}$$

where $R_\gamma^{NK}(T,\rho)$ is the rate of photons emitted from a thermal nuclear fragment with temperature T and density ρ (see Appendix A). From this model we have obtained that $R_\gamma^{NK}(T,\rho)$ scales with $\sim T^{6.7}$ and $\sim \rho$. The dependence of the photon rate on ρ^2 that one would expect classically turns to a ρ dependence due to the Pauli blocking. So, we can express the photon rate as $R_\gamma^{NK} \approx R_0^{NK} \cdot T^{6.7} \cdot \rho$.

We can simplify Eq. (8.2), assuming that the temperature is uniform in the volume V and constant during the emission time,

$$M_\gamma^{NK} \approx V \cdot \Delta\tau \cdot R_0^{NK} \cdot T^{6.7} \cdot \rho \tag{8.3}$$

where V and $\Delta\tau$ are respectively the volume and the lifetime of the radiating nuclear source. The volume can be approximated as the ratio between the sum of the projectile and target nucleons over the nuclear density, $V \approx (\mathrm{A}_t + \mathrm{A}_p)/\rho$. We do hence not consider the particle preequilibrium emission, which e.g. for the Xe+Sn reaction accounts for 15-25% of the system [49, 107]. Although the size of the excited fragment is not expected to follow an important evolution with the centrality [49], the preequilibrium emission might be less important for peripheral reactions. So, we have to keep in mind that taking the relative volume of the hard γ source as $(\mathrm{A}_t + \mathrm{A}_p)$ is a rough estimation.

Within these assumptions, the thermal hard photon yield, scaled to the relative size of the system, reads as:

$$\frac{M_\gamma^{NK}}{(A_t + A_p)} \approx \Delta\tau \cdot R_0^{NK} \cdot T^{6.7} \tag{8.4}$$

The former relation, which is independent of the density, can be therefore exploited to estimate the lifetime $\Delta\tau$ of the thermal equilibrated source, by comparing the behavior of the experimental multiplicities and the evolution of M_γ^{NK} with the temperature of the system. The calculated multiplicities successfully reproduce the experimental thermal hard photon yields measured for all the reactions (see Figs. 8.2 and 8.3), with $\Delta\tau$ values $\sim$ 100 fm/c which agree with the expected lifetime of an equilibrated source. This result confirms the validity of the thermal model, since it reproduces both experimental observables, the slope of the thermal hard photon spectrum and the thermal multiplicity, with the use of only one parameter, the temperature.

The inclusive thermal hard photon multiplicities measured as a function of T for the different reactions studied with TAPS suggest lifetimes $\Delta\tau \sim$ 100 fm/c (see Figure 8.3),

except for ^{86}Kr+^{58}Ni and ^{36}Ar+^{58}Ni at 60A MeV. For these two reactions, where the larger energies available in the nucleus-nucleus CM are reached, the M_γ^T are better reproduced by theoretical multiplicities emitted from shorter lived, $\Delta\tau \sim 35$ fm/c, equilibrated sources. This lifetime decrease might be connected with the fast fragmentation observed for high $\epsilon^\star$, and expected for spinodal decomposition [108]. The experimental thermal

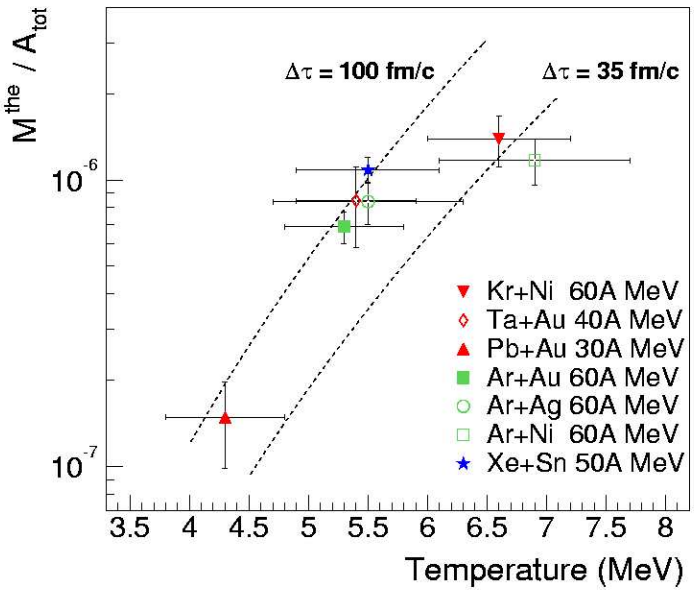

Figure 8.2: *Experimental thermal bremsstrahlung multiplicity, scaled to the size of the system $A_{tot} = A_t + A_p$, as a function of the extracted nuclear temperature, for the different reactions studied by the TAPS collaboration. The lines correspond to 2 different values of source lifetimes estimated within Eq. 8.4.*

hard photon multiplicities measured for the ^{129}Xe + ^{nat}Sn reaction classes exhibit a trend compatible with lifetimes on the order of 100-300 fm/c (Fig. 8.3). In our measurements we do not observe any change in the lifetime of the equilibrated fragment with the violence of the Xe+Sn collision. At variance with the short emission time estimated for the ^{86}Kr, ^{36}Ar+^{58}Ni reactions, $\Delta\tau$ of the most central Xe+Sn collisions identified in this work is totally compatible with $\Delta\tau$ observed for the rest of reaction classes. The estimated lifetime values, jointly with the measurement of an important production of thermal hard photons, point to the conclusion that at least for the investigated Xe+Sn reactions, the fireball does not undergo a simultaneous breakup from a diluted state.

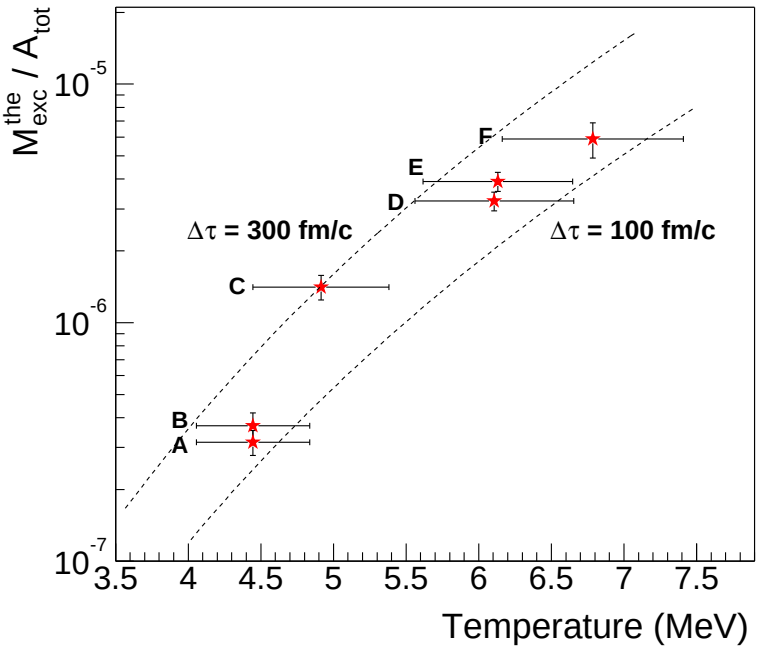

Figure 8.3: *Thermal hard photon multiplicity, scaled to the size of the system $A_{tot} = A_t + A_p$, as a function of the nuclear temperature extracted from Eq. (8.1), for the different ^{129}Xe + ^{nat}Sn reaction classes. Both lines correspond to 2 values of source lifetimes estimated within Eq. 8.4.*

8.3 Evolution of excitation energy with centrality

The caloric curve relates the temperature to the internal energy of excited systems in thermal equilibrium, $\epsilon^\star$ (A MeV). In order to construct the caloric curve of our studied system, the average excitation energy associated with each centrality reaction class must be evaluated. At variance with experiments performing energy measurements with charged particle detectors, we cannot determine $\epsilon^\star$ from our data. Fortunately, we can rely on the measurements of excitation energy carried out by the INDRA Collaboration. They have studied in detail the charged particle production in ^{129}Xe + ^{nat}Sn collisions at 50A MeV (see e.g. [43, 44, 45, 109, 100, 46]).

INDRA [110, 111] is a 4π multidetector dedicated to the detection of charged products emitted during heavy ion collisions. Fragments are identified in atomic number up to and better than Z=54 in the forward region. Beyond 45°, the charge resolution is one unit up

to Z $\approx$ 20. Over the whole angular range, isotopic identification is obtained for Z $\leq$ 4. The

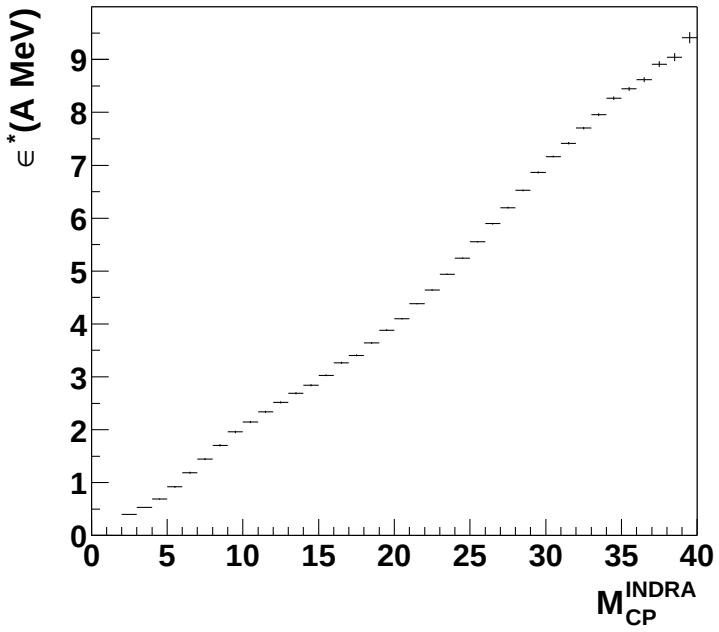

Figure 8.4: *Excitation energy per nucleon as a function of the charged particle multiplicity measured with INDRA in* ^{129}Xe + ^{nat}Sn *collisions at 50A MeV [112].*

excitation energy of Xe quasiprojectiles produced from peripheral to central collisions has been deduced by Steckmeyer *et al.*. The employed methods described in detail in [49] are based on the determination of the velocity of the quasiprojectile. They assume that all particles emitted in the forward hemisphere in the frame of the source are evaporated by the source, and that there is a forward backward symmetry. These assumptions, which rely on the isotropy of the angular distribution of particles in the forward hemisphere, are in complete agreement with the equilibration of the thermal hard photon source. The excitation energy is calculated from the kinetic energies of all products belonging to the source, i.e. employing the so-called "calorimetry" method:

$$\epsilon^{\star} = -Q + \sum_{i=1}^{M_{LCP}+M_{IMF}} K_i + \sum_{j=1}^{M_n} K_j + K_{Z_{max}} \tag{8.5}$$

where K_i, K_j and $K_{Z_{max}}$ are the kinetic energies of the ith charged particle, of the jth neutron, and of the QP residue, respectively. Q is the Q-value of the reaction. The neutron multiplicity is determined from mass conservation and the kinetic energy

of neutrons is estimated. In Figure 8.4 the obtained excitation energy is represented as

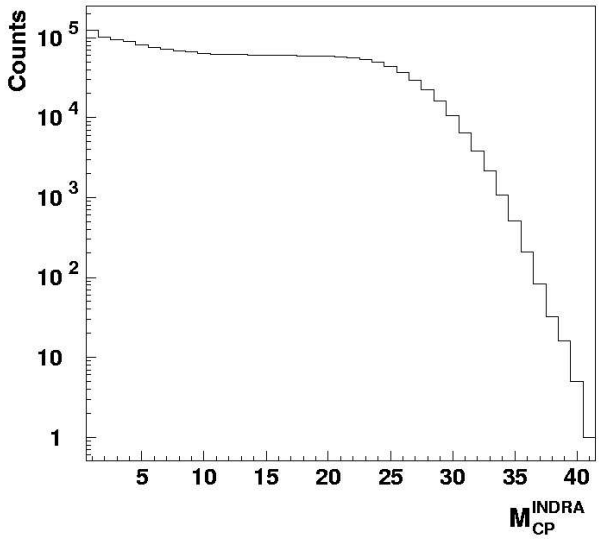

Figure 8.5: *Distribution of the charged particle multiplicity measured by INDRA in* $^{129}Xe + {}^{nat}Sn$ *collisions at 50A MeV [112].*

a function of the total charged particle multiplicity measured by INDRA, M_{cp}^{INDRA}. The excitation energy increases linearly with the violence of the collision up to a value between 9 and 11 MeV/nucleon. In collaboration with J.C. Steckmeyer, we have employed the geometric method previously described in 7.2.1, to relate the average impact parameter of each Xe + Sn reaction class with the corresponding value of M_{cp}^{INDRA} (Fig. 8.5), hence obtaining the $\epsilon^{\star}$. The M_{cp}^{INDRA} and $\epsilon^{\star}$ estimated for each reaction class are reported in Table 8.2. The $\epsilon^{\star}$ errors take into account the error derived from the $\langle b \rangle$ uncertainty, as well as the systematical uncertainty in the reconstruction of the quasiprojectile, which has been estimated as 10% of $\epsilon^{\star}$ [49]. The excitation energy exhibits a linear increase with the centrality (Fig. 8.6).

But concerning reaction class F, since as discussed in 7.3.1 the geometrical method used to relate $\langle b \rangle$ and M_{cp}^{INDRA} cannot be applied for central collisions, the reported excitation energy is just a rough estimation. So, for the representation of reaction class F in the caloric curve, we have used the value of $\epsilon^{\star}$ predicted for central collisions by the model of Natowitz *et al.* [113], $\epsilon^{\star} = (8.7 \pm 1.5)A$ MeV.

Reaction class	$\langle b \rangle$ (fm)	M_{cp}^{INDRA}	$\epsilon^{\star}(A$ MeV)
Inclusive	3.8 ± 1.0	25 ± 1	5.6 ± 1.0
A or Peripheral	7.6 ± 0.3	14 ± 1	2.8 ± 0.3
B	7.2 ± 0.3	16 ± 1	3.3 ± 0.4
C	4.2 ± 0.4	24 ± 1	5.2 ± 0.6
D	2.8 ± 0.4	27 ± 1	6.1 ± 0.7
E	2.2 ± 0.6	$29\ ^{+2}_{-1}$	6.7 ± 0.7
F or Central	1.0 ± 0.9	$32\ ^{+5}_{-2}$	$7.7\ ^{+1.4}_{-1.0}$

Table 8.2: *Values of the charged particle multiplicity measured with INDRA M_{cp}^{INDRA} and of the excitation energy estimated for each reaction class with averaged impact parameter $\langle b \rangle$.*

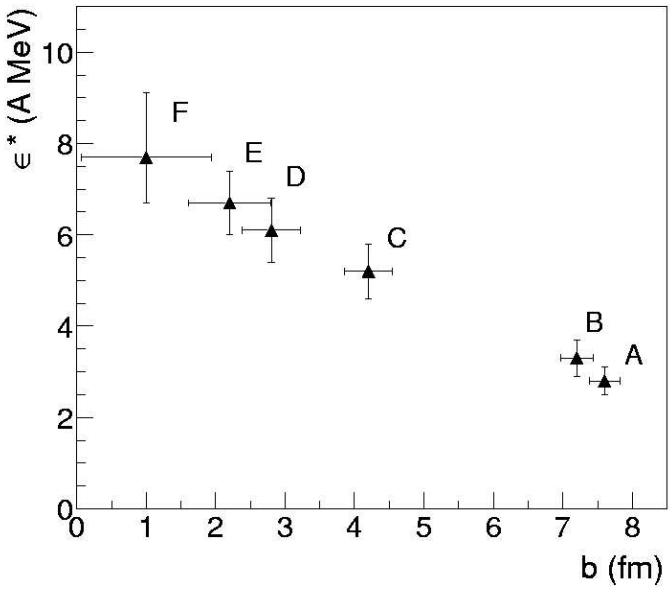

Figure 8.6: *Estimated excitation energy as a function of the experimental average impact parameter.*

8.4 Caloric curve

When a nuclear system of mass A is heated up to moderate excitation energies, where it still behaves as a degenerate Fermi liquid, the evolution of its excitation energy is governed

by a Fermi gas relation:

$$\epsilon^{\star} = \frac{E^{\star}}{A} = \frac{1}{K}T^2 \tag{8.6}$$

with the inverse level density parameter K = 8 - 13 MeV^{-1}.

However if the excited system is further heated up to high enough energies, it might undergo, as predicted, a liquid-gas phase transition. In the pure gas phase the $\epsilon^{\star}$ dependence on T is expected to turn into a Boltzmann gas relation, $\epsilon^{\star} \propto$ T. Therefore the construction of the nuclear caloric curve, which relates T and $\epsilon^{\star}$, is *a priory* the most direct tool to look for the existence of a thermally driven liquid-gas phase transition. The first caloric curve obtained in 1995 by the ALADIN collaboration [114] using a He-Li isotopic thermometer, exhibited 3 different regions: the already known Fermi-gas like temperature rise below $\epsilon^{\star} = 3A$ MeV, an almost constant temperature over the $\epsilon^{\star}$ range of 3-10A MeV, and then a sharp T increase up to $\epsilon^{\star} \approx 15A$ MeV. The intermediate plateau region has been interpreted as the latent heat associated with a first order phase transition ("boiling"). That first measurement encouraged many experiments, which however lead to contradictory results when directly comparing caloric curves based upon different particle thermometers, and from different reactions (for a recent review see [8]). Now, it is believed that data discrepancies might be eliminated if temperatures can be properly corrected for effects on the collision dynamics. Nevertheless, those temperature corrections are phenomenological and/or model dependent. Thus the reliance on more direct thermometers, as the photonic one, is of extremely importance in order to build self-consistent caloric curves.

8.4.1 Caloric curve constructed from the inclusive systematics

The caloric curve constructed by the TAPS Collaboration from the inclusive thermal hard photon slopes measured in 7 reactions, is clearly below the Fermi gas curve (see Fig. 8.7) [106]. The low T increase with $\epsilon^{\star}$ is in qualitative good agreement with a flattening behavior. Recently, Natowitz *et al.*[22] analyzed a wealth of data coming from many different experiments, where only temperatures corrected for preequilibrium and secondary emission have been considered. In this context they notice that the experimental caloric curves describe a consistent plateau behavior if different mass regions are considered. Concerning this result, the $\epsilon^{\star}$ reached in each collision studied by the TAPS Collaboration is above the starting point identified as the beginning of the plateau region in the analysis of Natowitz *et al.* [115]. They have observed that the limiting temperature decreases with the increase of the size of the system. This result has also been

predicted (e.g. [116]) and reproduced [117]. The relation of the temperatures measured by means of the photon thermometer with the system size is in a very good agreement with this behavior [118]. This independent analysis confirms hence the validity of the photon thermometer.

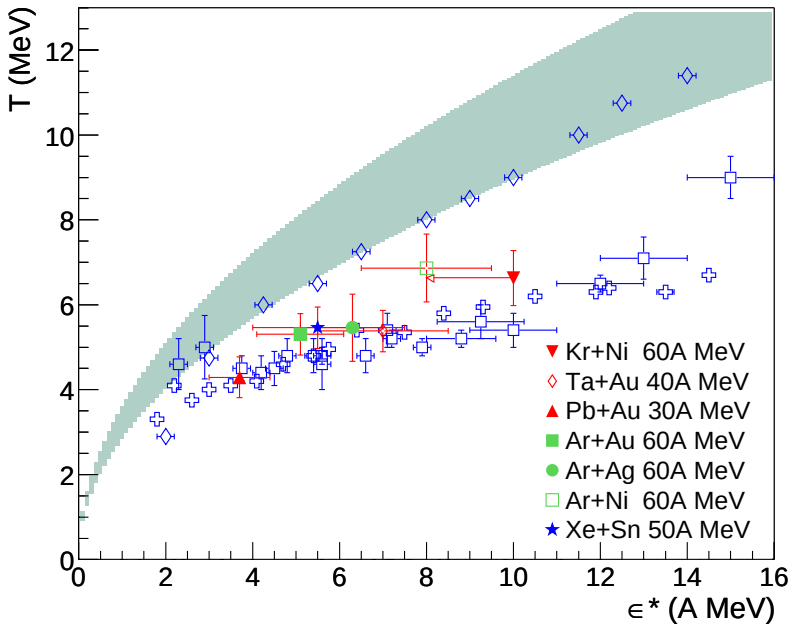

Figure 8.7: *Caloric curve constructed with the photon thermometer from inclusive TAPS measurements, compared to ALADIN (squares) EOS (crosses) curves (isotopic temperatures) and to INDRA (rhombbi) curve (kinetic temperatures). The dashed region corresponds to Fermi gas model curves from K=8 MeV^{-1} to K=13 MeV^{-1}. Adapted from [106].*

8.4.2 Caloric curve constructed from Xe + Sn exclusive measurements

The relationship between the estimated temperature and the excitation energy of the hot equilibrated fragment formed in the different centrality Xe + Sn reactions studied in this work is displayed in Fig. 8.8. The temperatures exhibit a smooth increase with the excitation energy, the estimated ($\epsilon^{\star}$,T) are below the Fermi fluid curves (for K=8,13 MeV^{-1}) . Peripheral reactions (classes A and B) lead to excitation energies near those identified as the onset of the plateau region: $\epsilon^{\star} \sim 3A$ MeV for A=180-241 [115].

By varying the centrality of the collision, instead of using several bombarding energies or systems, the obtained caloric curve should be more self consistent, since the extracted

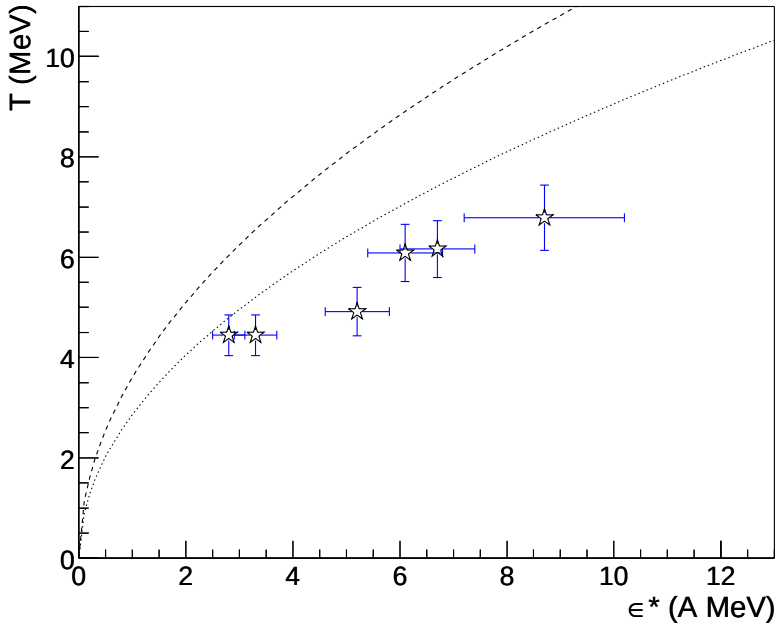

Figure 8.8: *Caloric curve constructed from the thermal hard photon slope measurements in the* $^{129}Xe + {}^{nat}Sn$ *reaction at 50A MeV, compared to the Fermi gas model curves for K=8* MeV^{-1} *(dashed line) and K=13* MeV^{-1} *(dotted line).*

temperatures have no uncertainties attributable to different experimental conditions or analysis procedures. However, aside the limited $\epsilon^{\star}$ range covered in a single reaction system and the difficulties to determine $\epsilon^{\star}$(b), a possible drawback, mostly in the case of very peripheral collisions, is the uncertainty in the mass of the equilibrated composite system.

Chapter 9

Summary and Outlook

9.1 Summary

In this thesis we present the analysis of the E300 heavy ion experiment, performed by the TAPS Collaboration in 1998 at the GANIL facility. The nuclear bremsstrahlung in ^{129}Xe + ^{nat}Sn reactions at 50A MeV is investigated. Emphasis is put on the measurement of a thermal hard photon component, emitted in secondary proton-neutron bremsstrahlung collisions, as a function of the centrality of the collision. The hard photon emission is studied both inclusively and exclusively, exploiting the performance of a complete detection system composed of the TAPS photon spectrometer coupled for the first time with three different charged-particle multidetectors: the GANIL "Silicon Strip Detector", the Washington University "Dwarf Ball" and the KVI "Forward Wall".

The measured inclusive hard photon spectrum consists of a direct component, emitted during the preequilibrium stage of the reaction, plus a later thermal component, accounting for 78 % and 22 % of the total hard-photon yield, respectively.

- The inverse slope parameter and probability of the direct component, E_0^d=(15.6 $\pm$ 1.0) MeV and P_γ=(7.83 $\pm$ 0.70) $\cdot$ 10^{-4}, follow the well known dependence on the bombarding energy.

- The inverse slope of the thermal component, E_0^t=(7.0 $\pm$ 0.6) MeV, scales with the available energy in the nucleus-nucleus center of mass E_{Cc}^{AA}. Consistently, the systematics of the thermal bremsstrahlung multiplicity normalized to the system size also scales with E_{Cc}^{AA}. These results are fully compatible with results obtained

from the former TAPS campaign at KVI[42], confirming hence that the thermal hard photon component emerges from a thermally equilibrated source.

The high statistics of the experiment in concomitance with the complete set-up have enabled to undertake for the first time a systematic exclusive investigation on thermal hard photon production.

- A thermal hard photon emission has been measured along all the covered impact parameter range ($0.1 \leq b/b_{max} \leq 0.6$). The thermal contribution to the total hard photon production amounts from 19% for the most peripheral collisions, up to 27% for the central ones.

- The measured thermal hard photon slope increases with the number of first-chance *pn* collisions. This behavior is consistent with the linear dependence of the inclusive thermal hard photon slope on the available energy in the nucleus-nucleus center of mass, observed for reactions where a thermal hard photon is detected.

- Whereas the variation of the direct hard photon yield with the centrality does not depend on the direct hard photon slope, the exclusive thermal multiplicity and slope values are linearly correlated (Fig. 7.11). That is a clear evidence of the sensibility of the thermal bremsstrahlung emission to the temperature of the source.

- The hard photon spectrum for the particular reactions identified as multifragmentation events also features a thermal component, whose characteristics are fully compatible with the ones measured for the inclusive spectra. Nevertheless, due to limitations of our setup, the identified multifragmentation reactions correspond only to a small fraction of semicentral reactions.

- We have compared the GDR spectra estimated for the most peripheral Xe+Sn centrality classes with the GDR distribution measured by the MEDEA Collaboration [92] for ^{36}Ar + ^{90}Zr reactions at 27A MeV. The excellent agreement between the GDR yields observed in both reactions has allowed to discard any contamination due to the GDR decay component in the low energy part of the peripheral Xe+Sn hard photon spectra.

The measurement of a thermal *pn* bremsstrahlung flash has been exploited to probe the thermodynamical state of excited nuclear matter in thermal equilibrium.

- The temperature of the composite system has been extracted from the measured thermal hard photon slope, applying the thermal model of Neuhauser and Koonin. The temperature measured for Xe+Sn reactions exhibits an increasing behavior (4.4 $\rightarrow$ 6.8 MeV) from the most peripheral reaction class ($b/b_{max} \approx 0.6$) to the most central reaction class ($b/b_{max} \leq 0.1$).

- The bremsstrahlung multiplicities calculated by means of the thermal model successfully reproduce the experimental measurements for all the investigated reactions (Figs. 8.2 and 8.3), for emission times which agree with the expected lifetime for equilibrated excited nuclei. Along the covered centrality range, no change in the lifetime of the equilibrated fragment with the violence of the Xe+Sn collision has been observed.

- The excitation energy measurements performed by the INDRA Collaboration [49] have been employed to estimate the excitation energy corresponding to each centrality Xe+Sn class, the obtained values are in the region of $\epsilon^{\star} \approx$ 2.8-8.7 MeV.

- Finally, we have constructed the first caloric curve from exclusive thermal hard photon measurements. The obtained curve falls below the one expected for a Fermi fluid (Fig.8.8). This result is in good agreement with the behavior observed from the inclusive thermal hard photon slopes (Fig. 8.7).

9.2 Outlook

Once we have developed the procedure to study the thermal bremsstrahlung emission, we pretend to analyze the hard photon spectra for more selective centrality classes of the same reaction, in particular we will try to measure an "analyzable" hard photon spectrum for still more peripheral reactions than the one identified in the present analysis. A similar exclusive analysis might be carried out for the ^{36}Ar+^{197}Au reaction at 60A MeV of the TAPS campaign at KVI. From both experiments it has been shown that the thermal hard photon signal should be a precious observable that can extend and provide complementary physics results in dedicated multifragmentation studies.

Besides the experimental problems which have to be faced to determine the nuclear temperatures (and excitation energies), it should be kept in mind that the caloric curve is just a projection of the bidimensional equation of state, depending on both temperature and density, ϵ(T,ρ). Therefore, changes in the shape of one-dimensional caloric curves

should only be taken into account when the ($\epsilon^{\star}$,T) points have been extracted within similar density conditions. That might be accomplished if we would be able to build a complete systematics, i.e. fully covering a mass region, of caloric curves with the γ thermometer. In order to emit measurable bremsstrahlung from second chance NN collisions, the source density must not be far from the saturation value. Nevertheless, if at given T,ρ conditions the system fragments from a diluted system, no thermal radiation should be emitted. Finally, we want to stress that we do not propose the use of the thermal bremsstrahlung emission as the *only* experimental tool but as an observable that can extend and provide complementary physics results related to the liquid-gas phase transition.

Appendix A

Thermal model

In the last Chapter we determined the temperature of the nuclear fireball formed in ^{129}Xe + ^{nat}Sn reactions, from the slope of experimental thermal hard photon spectra, E_0^t. The relation between T and E_0^t (Eq. 8.1) is derived from the thermal model of Neuhauser and Koonin [105]. Within a thermal picture, each volume of space-time occupied by hadrons during the collision emits photons at a rate depending on its local conditions (density, temperature, etc.), and the final experimental spectrum is the superposition of these many incoherent contributions. However, due to the weak photon-hadron coupling, the emitted photons are not in thermal equilibrium with the hadrons. Hence, the spectrum of photons emitted from a given volume is mostly determined by the nature of the elementary nucleon-nucleon collision processes that occur within it. The thermal model of Neuhauser and Koonin assumes that, neglecting the coherent current, the rate of nucleon-nucleon bremsstrahlung emitted within a hot nuclear fragment in thermal equilibrium, reads as:

$$\frac{d^5N_\gamma}{d^3x\,dt\,dE_\gamma} = \frac{8}{4\pi}\int \frac{d\vec{p}_{1i}}{(2\pi)^3}\frac{d\vec{p}_{2i}}{(2\pi)^3}\, f(\vec{p}_{1i})f(\vec{p}_{2i})\,\beta_{12i}\,\frac{d\sigma}{dE_\gamma} \tag{A.1}$$

where $\vec{p}_{1,2i}$ and β_{12i} are the initial momenta and relative-velocity of the colliding nucleons, $f(\vec{p})$ the single-particle momentum distribution, and $d\sigma/dE_\gamma$ the angle-integrated Pauli-blocked nucleon-nucleon bremsstrahlung cross-section.

Approximating the emitting region as a piece of nuclear matter in thermal equilibrium with local temperature T and density ρ, the momentum distribution can be parameterized by a hot Fermi-Dirac distribution:

$$f(\vec{r},\vec{p}) = \frac{1}{1+exp\left(\left[\sqrt{p^2+m_N^2}-E_F(\rho)\right]/T\right)} \tag{A.2}$$

normalized to:

$$4\int \frac{d\vec{p}}{(2\pi)^3} f(\vec{p}) = n \tag{A.3}$$

where n is the nucleon number density. For low temperatures the chemical potential μ of a system of nucleons can be written as a function of the Fermi energy $\epsilon_F(\rho)$ and T:

$$\mu(\rho) \;\approx\; \epsilon_F(\rho)\left\{1-\frac{\pi^2}{12}\left[\frac{T}{\epsilon_F(\rho)}\right]^2\right\} \quad \text{when} \quad T \ll \epsilon_F \tag{A.4}$$

The angle-integrated Pauli-blocked nucleon-nucleon bremsstrahlung cross-section $d\sigma/dE_\gamma$ of Eq. (A.1) can be approximated (assuming isotropic pn scattering) by:

$$\frac{d\sigma}{dE_\gamma} \approx \frac{d\sigma_{free}}{dE_\gamma}\int \left[1-f(\vec{p}_{1f})\right]\left[1-f(\vec{p}_{2f})\right]\frac{d\Omega_\gamma}{4\pi}\frac{d\Omega_f}{4\pi} \tag{A.5}$$

where $d\sigma_{free}/dE_\gamma$ is the elementary nucleon-nucleon bremsstrahlung cross-section in free space, and $d\Omega_{\gamma,f}$ are the solid angle of the outgoing photon and nucleons. Since the ppγ process can be neglected at Fermi energies, the isospin averaged $d\sigma_{free}/dE_\gamma$ is one half of the elementary $pn\gamma$ differential cross-section, which here has been taken as the covariant Schäfer parameterization [119]. The thermal pn bremsstrahlung rate of Eq. (A.1) can be therefore calculated for a thermal equilibrated source of temperature T and density ρ (see example of Fig. A.1). The model hard photon spectra can be well approximated

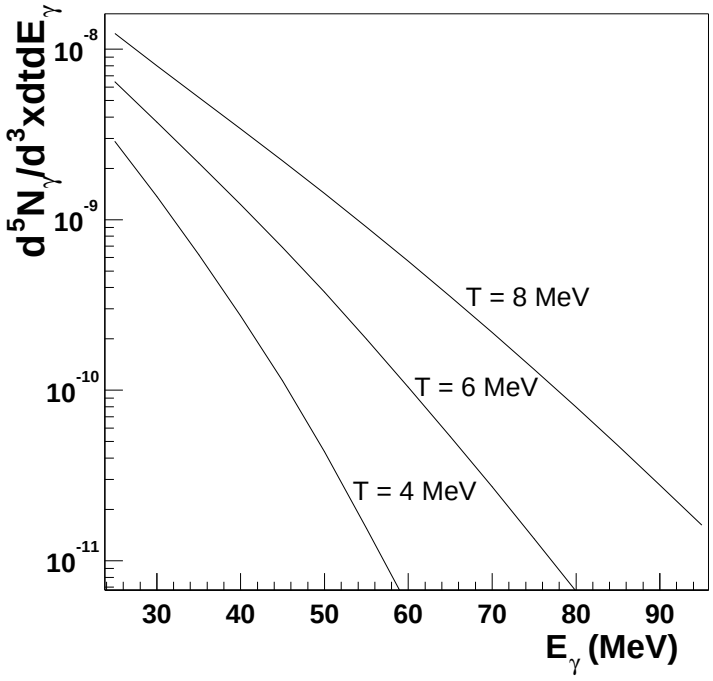

Figure A.1: *Thermal bremsstrahlung ($pn\gamma$) emission rates, from a nuclear system in thermal equilibrium at the saturation density $\rho_0 = 0.17\ fm^{-3}$ for various temperatures ($T = 4$ MeV, $T = 6$ MeV and $T = 8$ MeV). From [26].*

by a single exponential E_0^t in agreement with the experimental data. The integrated bremsstrahlung ($pn\gamma$) yields are found to scale approximately with $T^{6.7}$ and ρ. The E_0^t extracted from the fit of the theoretical spectra are found to be linearly related with the temperature T of the emitting source according to Eq. (8.1).

System	K_{lab} (MeV)	E_{Cc}^{AA} (MeV)	E_0^t (MeV)	T (MeV)	M_γ^{NK} (10^{-4})	M_γ^{exp} (10^{-4})	$\epsilon^\star$ (A MeV)
^{208}Pb+^{197}Au	30	6.0	5.5 ± 0.6	4.3 ± 0.5	0.7 ± 0.7	0.6 ± 0.2	3.7 ± 0.7
^{36}Ar+^{197}Au	60	7.1	6.8 ± 0.6	5.3 ± 0.5	1.9 ± 1.3	1.6 ± 0.2	5.1 ± 1.0
^{181}Ta+^{197}Au	40	8.6	6.9 ± 0.6	5.4 ± 0.5	3.4 ± 1.9	3.2 ± 1.0	7.0 ± 1.5
^{36}Ar+^{107}Ag	60	10.6	7.0 ± 1.0	5.5 ± 0.8	1.5 ± 1.5	1.2 ± 0.2	6.3 ± 1.2
^{86}Kr+^{58}Ni	60	11.2	8.5 ± 0.8	6.6 ± 0.6	4.4 ± 2.7	2.0 ± 0.4	< 10
^{36}Ar+^{58}Ni	60	13.2	8.8 ± 1.0	6.9 ± 0.8	4.1 ± 2.9	1.1 ± 0.2	8.0 ± 1.5
^{129}Xe+^{112}Sn	50	13.4	7.0 ± 0.6	5.5 ± 0.5	3.1 ± 2.2	2.6 ± 0.3	7.0 ± 1.5

Table A.1: *Nuclear temperatures T estimated through Eq. (8.1) from the experimental thermal hard photon slopes E_0^t of the inclusive hard photon spectra measured by the TAPS Collaboration. Adapted from [106].*

Appendix B

Dwarf Ball miscellanea

Table B.1: *Dwarf-Ball telescope positions and thicknesses of their CsI(Tl) and plastic scintillators.*

# Detector	θ [°]	ϕ [°]	E (mg/cm^2)	ΔE (mg/cm^2)
1	41.59	230.02	8.08	4.08
2	41.59	302.02	8.38	4.07
3	41.59	14.02	8.20	4.06
4	41.59	86.02	8.33	4.05
5	41.59	158.02	8.20	4.03
6	49.51	191.73	8.13	3.98
7	49.51	263.73	8.20	3.97
8	49.51	335.73	8.28	3.95
9	49.52	47.73	8.41	3.93
10	49.51	119.73	8.33	3.92
11	63.43	216.00	4.34	3.89
12	63.43	288.00	4.39	3.87
13	63.43	0.00	4.37	3.86
14	63.43	72.00	4.31	3.84
15	63.43	144.00	4.34	3.81
16	67.93	242.39	4.04	3.80
17	67.93	314.39	4.32	3.79
18	67.93	26.39	4.24	3.76
19	67.93	98.39	4.34	3.76
20	67.93	170.39	4.27	3.73
21	77.52	194.74	4.06	3.72
22	77.52	266.74	4.42	3.68
23	77.52	338.74	4.27	3.65
24	77.52	50.74	4.32	3.65
25	77.52	122.74	4.22	3.62
26	87.30	221.39	4.37	3.50
27	87.30	293.39	4.12	3.50
28	87.30	5.39	4.34	3.50
29	87.30	77.39	4.??	3.50
30	87.30	149.39	4.??	3.50
31	92.70	246.61	4.37	3.50
32	92.70	318.61	4.34	3.49
33	92.70	30.61	4.27	3.49
–	92.70	102.61	–	

Table B.1: (continuation)

# Detector	θ [°]	ϕ [°]	E (mg/cm^2)	ΔE (mg/cm^2)
34	92.70	174.61	4.32	3.42
35	102.48	201.26	4.27	3.39
36	102.48	273.26	4.06	3.38
37	102.48	345.26	4.34	3.37
38	102.48	57.26	4.24	3.34
39	102.48	129.26	4.??	3.32
40	112.07	225.61	4.32	3.30
41	112.07	297.61	4.29	3.30
42	112.07	9.61	4.32	3.26
43	112.07	81.61	4.12	3.23
44	112.07	153.61	4.24	3.21
45	116.57	180.00	3.96	3.18
46	116.57	252.00	4.22	3.17
47	116.57	324.00	4.32	3.13
48	116.57	36.00	4.34	3.12
49	116.57	108.00	4.06	3.11
50	130.49	204.27	4.24	3.04
51	130.49	276.27	4.17	3.04
52	130.49	348.27	4.22	3.04
53	130.49	60.27	4.29	3.02
54	130.49	132.27	4.34	3.00
55	138.41	237.98	3.99	2.98
56	138.41	309.98	4.37	2.97
57	138.41	21.98	4.32	2.95
58	138.41	93.98	4.28	2.94
59	138.41	165.98	4.32	2.92
60	155.58	202.89	4.32	2.83
61	155.58	274.89	4.37	2.83
62	155.58	346.89	4.34	2.83
63	155.58	58.89	4.24	2.80
64	155.58	130.89	4.34	2.11

Bibliography

[1] H. Jaqaman, A. Z. Mekjian, and L. Zamick, Phys. Rev. **C27**, 2782 (1983).

[2] P. Siemens, Nucl. Phys. **A428**, 189c (1984).

[3] J. Lattimer and M. Prakash, Astrophys. J. (2001).

[4] C. Ishizuka *et al.*, nucl-th/0208020 .

[5] P. Braun-Munzinger, Nucl. Phys. (2001).

[6] W. Bauer *et al.*, Nucl. Phys. **A553**, 749 (1993).

[7] L. G. Moretto and G. J. Wozniak, Ann. Rev. Nucl. Part. Sci. **43**, 379 (1993).

[8] M. B. T. S. Das Gupta, A. Z. Mekjian, nucl-th/0009033 (2001).

[9] M. Baldo *et al.*, Phys. Rev. Lett **C51**, 1 (1995).

[10] L. G. Moretto *et al.*, Phys. Rev. Lett **70**, 372 (1996).

[11] D. Gross, Nucl. Inst. and Meth. **A553**, 175 (1993).

[12] A. Botvina *et al.*, Nucl. Phys. **A475**, 663 (1987).

[13] J. P. Bondorf *et al.*, Phys. Rept. **257**, 133 (1995).

[14] J. Aichelin, Phys. Rept. **202**, 233 (1991).

[15] J. A. R. Nebauer and the INDRA Collaboration, Nucl. Phys. **A658**, 67 (1999).

[16] O. Tirel *et al.*, nucl-ex/9810001 .

[17] P. J.Richert, Phys. Rept. **350**, 1 (2001).

[18] J. Elliott *et al.*, Phys. Rev. **C67**, 024609 (2003).

[19] J. Elliott *et al.*, Phys. Rev. Lett. **88**, 042701 (2002).

[20] A. C. J. Pochodzalla, Proceedings of the 1st Catania Relativistic Ion Studies nucl (1996).

[21] J. Pochodzalla, Prog. Part. Nucl. Phys. **39**, 443 (1997).

[22] J. B. Natowitz *et al.*, Phys. Rev. **C65**, 034618 (2002).

[23] M. D'Agostino *et al.*, Phys.Lett. **B473**, 219 (2000).

[24] P. Chomaz, Proceedings of the INPC 2001 Conference, Berkeley, Ca., 3512 (2001).

[25] Y. Schutz *et al.*, Nucl. Phys. **A622**, 405 (1997).

[26] D. d'Enterria, Ph.D. thesis, Univ. de Caen and Univ. Autònoma de Barcelona, 2000.

[27] E. Grosse, Workshop on Gross Properties of Nuclei and Nuclear Excitation (GSI, Darmstad) (1985).

[28] K. Beard *et al.*, Phys. Rev. **C32**, 1111 (1985).

[29] J. Stevenson *et al.*, Phys. Rev. Lett. **57**, 555 (1986).

[30] N. Alamanos *et al.*, Phys. Lett. **B173**, 392 (1986).

[31] H. Nifenecker, Prog. Part. Nucl. Phys. **23**, 271 (1989).

[32] H. Nifenecker and J. Pinston, Ann. Rev. Nucl. Part. Sci. **40**, 113 (1990).

[33] W. Cassing *et al.*, Phys. Rept. **188**, 363 (1990).

[34] J. van Pol, Ph.D. thesis, Rijksuniversiteit Groningen, 1995.

[35] R. Bertholet *et al.*, Nucl. Phys. **A474**, 541 (1987).

[36] H. Nifenecker and J. Bondorf, Nucl. Phys. **A442**, 478 (1985).

[37] J. Jackson, *Classical Electrodynamics* (John Wiley & Sons, NY, 1975).

[38] F. Marqués *et al.*, Phys. Lett. **B349**, 30 (1995).

[39] F. Marqués *et al.*, Phys. Rept. **284**, 91 (1997).

[40] G. Martínez *et al.*, Phys. Lett. **B349**, 23 (1995).

[41] Y. Schutz, Acta Phys. Polon. **B27**, 263 (1996).

[42] D. d'Enterria *et al.*, Phys. Rev. Lett. **87**, 22701 (2001).

[43] N. Marie, Ph.D. thesis, Université de Caen, 1995.

[44] N. Marie, Phys. Lett. **B391**, 15 (1997).

[45] N. Marie *et al.*, Phys. Rev. **C58**, 256 (1998).

[46] N. L. Neindre, Ph.D. thesis, Université de Caen, 1999.

[47] D. Gourio *et al.*, Eur. Phys. J. **A7**, 245 (2000).

[48] N. Bellaize *et al.*, Nucl. Phys. **A709**, 367 (2002).

[49] J. Steckmeyer *et al.*, Nucl. Phys. **A583**, 461 (2001).

[50] http://www.ganil.fr/operation/availablebeams/.

[51] H. Ströher, Nucl. Phys. News **6**, 7 (1996).

[52] *The first 10 years with TAPS* (Universität Gießen, Gießen, 1997).

[53] A. Gabler *et al.*, Nucl. Inst. and Meth. **A346**, 168 (1994).

[54] G. Knoll, *Radiation Detection and Measurements* (John Wiley & Sons, NY, 1989).

[55] R. Novotny *et al.*, Nucl. Inst. and Meth. **A262**, 340 (1987).

[56] M. Laval *et al.*, Nucl. Inst. and Meth **206**, 69 (1983).

[57] G. Gratta *et al.*, Ann. Rev. Nucl. Part. Sci. **44**, 453 (1994).

[58] R. Novotny, IEEE Trans. Nucl. Sci. **NS-38**, 379 (1991).

[59] T. Matulewicz *et al.*, Nucl. Inst. and Meth. **A289**, 194 (1990).

[60] T. Davisdon *et al.*, Nucl. Inst. and Meth **A288**, 245 (1990).

[61] S. L. Thomas *et al.*, Nucl. Inst. and Meth **A288**, 212 (1990).

[62] D. Stracener *et al.*, Nucl. Inst. and Meth. **A294**, 485 (1990).

[63] D. Wilkinson, Rev. Sci. Inst. **23**, 414 (1952).

[64] C. Caso *et al.*, Eur. Phys. J. **C3**, 1 (1998).

[65] http://blast02.lns.mit.edu/targets/ion/manuals.

[66] S. Luke *et al.*, Phys. Rev. C **47**, 1211 (1993).

[67] http://www.wnes.net/.

[68] A. Wuosmaa *et al.*, Nucl. Inst. and Meth **A345**, 482 (1994).

[69] http://www.in2p3.fr/CC/.

[70] http://www-subatech.in2p3.fr/ photons/taps/foster/.

[71] http://www.info.cern.ch/asd/paw.

[72] http://www-subatech.in2p3.fr/ photons/taps/rosebud/.

[73] L. Aphecetche, Ph.D. thesis, Université de Caen, 1998.

[74] R. Brun and F. Rademakers, Nucl. Inst. and Meth. **A389**, 81 (1997).

[75] J. Wilson, *Cosmic Rays* (The Wikeham Science Series, London, 1976).

[76] R. Barnett, Phys. Rev. **D54**, 1 (1996).

[77] M. Hoefman, Ph.D. thesis, Rijksuniversiteit Groningen, 1999.

[78] T. Matulewicz, Nucl. Inst. and Meth. **A325**, 365 (1993).

[79] G. Martínez *et al.*, Nucl. Inst. and Meth. **A391**, 435 (1997).

[80] T. Awes *et al.*, Nucl. Inst. and Meth. **A311**, 130 (1992).

[81] C. A. Group, *GEANT Detector Description and Simulation Tool*, w5013 ed., CERN, Geneva, 1993.

[82] M. Marqués, Ph.D. thesis, Universitat de València, 1994.

[83] G. Martínez, Ph.D. thesis, Universitat de València, 1994.

[84] H. Bethe, Rev. Mod. Phys. **9**, 69 (1937).

[85] L. Tassan-Got, Nucl. Inst. Meth. **B194**, 503 (2002).

[86] M. Mora, Master's thesis, Universidad de Salamanca, 2000.

[87] M. Josset, Ph.D. thesis, Univ. de Caen, 1996.

[88] C. Tam *et al.*, Phys. Rev. **C39**, 1371 (1989).

[89] L. Aphecetche *et al.*, GANIL report **R9702**, 1 (1997).

[90] G. Fai and J. Randrup, Comput. Phys. Commun. **42**, 385 (1986).

[91] R. Alba *et al.*, Nucl. Phys. **A654**, 761 (1999).

[92] T. Suomijärvi *et al.*, Phys. Rev. **C53**, 2258 (1996).

[93] P. Piatelli *et al.*, Nucl. Phys. **A599**, 63 (1996).

[94] C. Cavata *et al.*, Phys. Rev. **C42**, 1760 (1990).

[95] M. Kwato-Njock *et al.*, Nucl. Phys. **A489**, 368 (1988).

[96] S. Riess *et al.*, Phys. Rev. Lett. **69**, 1504 (1992).

[97] E. Migneco *et al.*, Phys. Lett. **B298**, 46 (1993).

[98] D. Santonocito *et al.*, Phys. Rev. **C66**, 044619 (2002).

[99] R. Stock, Phys. Rev. Lett. **44**, 1243 (1980).

[100] J. Benlliure, Ph.D. thesis, Universitat de València, 1995.

[101] V. Metivier, Ph.D. thesis, Université de Caen, 1995.

[102] G. Martínez *et al.*, Phys. Lett. **B334**, 23 (1994).

[103] J. J. Gaardhoje *et al.*, Phys. Rev. Lett. **59**, 1409 (1987).

[104] J. L. Faou *et al.*, Phys. Rev. Lett. **72**, 3321 (1994).

[105] D. Neuhauser and S. Koonin, Nucl. Phys. **A462**, 163 (1987).

[106] D. d'Enterria *et al.*, Phys. Rev. Lett. **B538**, 27 (2002).

[107] J. B. Natowitz *et al.*, Phys. Rev. **C52**, R2322 (1995).

[108] L. Beaulieu *et al.*, Phys. Rev. Lett. **84**, 5971 (2000).

[109] J. Lukasik *et al.*, Phys. Rev. **C55**, 1906 (1997).

[110] J. Pouthas *et al.*, Nucl. Inst. and Meth. **A357**, 418 (1995).

[111] J. Pouthas *et al.*, Nucl. Inst. and Meth. **A369**, 222 (1996).

[112] J. Steckmeyer, Private comunication .

[113] J. B. Natowitz *et al.*, Z. Phys. A **325**, 467 (1986).

[114] J. Pochodzalla *et al.*, Phys. Rev. Lett. **75**, 1040 (1995).

[115] J. B. Natowitz *et al.*, nucl .

[116] P. Bonche *et al.*, Nucl. Phys. **A436**, 265 (1985).

[117] C. D. A. Barrañón, J.A. López, Contribution for the National Congress of the Sociedad Mexicana de Fisica at Leon (Mexico) **nucl-th/0301001**, 3512 (2002).

[118] J. B. Natowitz *et al.*, Phys. Rev. Lett. **89**, 212701 (2002).

[119] M. Schäfer *et al.*, Z. Phys. **A339**, 391 (1991).

List of Figures

List of Tables